JPL D-28534

Earth Observing System (EOS)

Microwave Limb Sounder (MLS) Mesosphere-Specific Forward Model Algorithm Theoretical Basis Document

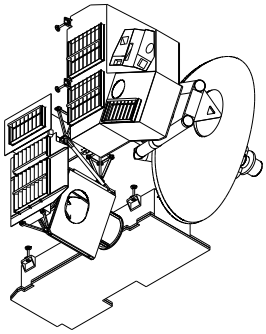

Michael J. Schwartz
W. Van Snyder
William G. Read

Version 1.0
June 15, 2004

National Aeronautics and
Space Administration

Jet Propulsion Laboratory
California Institute of Technology
Pasadena, California

Contents

This algorithm theoretical basis document (ATBD) addresses issues that are of concern in the retrieval of atmospheric parameters from the highest altitudes scanned by EOS-MLS. Its primary purpose is to supplement the *EOS MLS Forward Model ATBD* [10] with a theoretical basis for polarized radiative transfer in the vicinity of the the Zeeman-split, 118-GHz O_2 line.

Although we are interested only in the radiances for the polarization of the MLS receiver being modeled, radiative transfer modeling of resolved, Zeeman-split lines requires calculation of radiance in both polarizations and of the correlation between the two modes. The goal here is to provide a module for polarized radiative transfer that can be dropped into the context of the scalar forward model production code. The polarization of the receiver in question (R1A or R1B) can be selected from the matrix output of the polarized code, and provides a grid of monochromatic radiances for discrete pointings that can be convolved in frequency and pointing by the existing scalar code.

Frequency convolution for the EOS-MLS digital autocorrelator spectrometers (DACS) is described in a separate chapter of this document. The DACS are considered to be a "Mesospheric" issue because they measure signals from the Doppler-broadened cores of O_2, H_2O, CO and O_3, which originate in the Mesosphere and above.

The first two chapters are pedagogical reviews of the microwave spectroscopy of oxygen and the origins of the polarized radiative transfer equation for a slightly anisotropic medium. The meat of the algorithms for MLS follows.

Chapter 1

Spectroscopy

1.1 The 118-GHz O_2 Spectral Line

Diatomic oxygen has a band of spectral lines near 60 GHz, an isolated line at 118.75 GHz, and a series of higher-frequency lines in the sub-millimeter, which are all magnetic-dipole transition resulting from the realignment of the molecule's dumbbell rotation and its electronic spin. Under atmospheric conditions, diatomic oxygen is well modeled as a rigid rotator in its electronic ground state. In units of energy scaled by the Boltzmann constant, the first vibrational levels of $^{16}O_2$ is 2239K above the vibrational ground state and the first electronic excited state, $^1\Delta_g$, is 10,200K above the electronic ground state. These excited states are largely frozen out at atmospheric temperatures under the assumption of local thermodynamic equilibrium.

1.1.1 Diatomic Oxygen Electronic Ground State

The electronic ground state of diatomic oxygen (O_2) is $^3\Sigma_g^-$. This notation denotes that

- it has zero electronic orbital angular momentum (Σ),
- it has electronic spin of one from two unpaired electrons, making it a triplet state (superscript 3),
- it is odd under reflection of the electrons through a plane containing the two nuclei (superscript "-"),
- it is even under inversion of the electrons through the midpoint of the internuclear axis (g from the German *gerade*).

This combination makes the electronic state odd under exchange of the nuclei, limiting allowed rotational states when the nuclei are identical, as discussed in Section 1.1.3.

1.1.2 O_2 Spin-Rotational States

The spin-rotational Hamiltonian of O_2 contains terms involving the angular momentum of the rigid rotation of the molecule, $\boldsymbol{N}$, the interaction between the two spins that make up

total electronic spin, $\boldsymbol{s}$, and the coupling of $\boldsymbol{J}$ and $\boldsymbol{s}$.

$$\begin{aligned} \mathcal{H} &= B(\boldsymbol{N}^2)/\hbar^2 &+\lambda(s_z^2 - \tfrac{1}{3}\boldsymbol{s}^2)/\hbar^2 &+\gamma(\boldsymbol{N}\cdot\boldsymbol{s})/\hbar^2 \\ &= \mathcal{H}_{\text{rot}} &+\mathcal{H}_{\text{spin-spin}} &+\mathcal{H}_{\text{spin-rot}}. \end{aligned} \tag{1.1}$$

Angular momentum is not strongly coupled to the intermolecular axis, since there is no electronic orbital angular momentum, and the Hamiltonian is dominated by $\mathcal{H}_{\text{rot}}$ for all but the lowest rotational states of $\boldsymbol{N}$. Thus, the O_2 states are best approximated as Hund's case (b), where $\boldsymbol{N}$ and $\boldsymbol{s}$ add vectorially to give total angular momentum, $\boldsymbol{J}$, as is shown in Figure 1.1. In this ideal coupling case, N is a good quantum number and $\mathcal{H}_{\text{rot}} = BN(N+1)$ is diagonal with $B = 43.1$GHz. In Hund's case (b), $\boldsymbol{J}$, and (N, s, J, m) are good quantum numbers. The magnitudes of $\boldsymbol{N}^2$, $\boldsymbol{s}^2$ and $\boldsymbol{J}^2$ are $N(N+1)\hbar^2$, $s(s+1)\hbar^2$, $J(J+1)\hbar^2$ respectively. The projection of $\boldsymbol{J}$ on an external axis, which we will take to be the direction of the geomagnetic field, is $m\hbar$. In the case of the oxygen ground state, $s = 1$, and J can take positive values $N-1$, N, $N+1$.

The spin-spin term (also called "pseudo-quadrupole" because of its resemblance to a nuclear quadrupole term) depends upon the projection of electronic spin upon the internuclear axis. This term results from the interaction between the two electronic spin $\frac{1}{2}$'s, and also from the partial excitement of electrons into Π orbits by the electronic magnetic moments. This term's diagonal element is zero for $J = N$ states and approaches -59.5 GHz for the $J = N+1$ and $J = N-1$ states with large values of N. For the ($N = 1$, $J = 0$) state, it is approximately 119 GHz. This term is what makes the states with $J = N \pm 1$ approximately 60 GHz lower than those with $J = N$, giving rise to the 60 GHz oxygen band, and it causes the ($J = 1$, $N = 1$) to ($J = 0$, $N = 1$) transition to be near 119 GHz.

The spin-spin term is not diagonal in the Hund's case (b) basis, but the Hund's (b) states provide a basis in which the Hamiltonian can be diagonalized. The resulting eigenstates are close to Hund's (b), and are labeled by the Hund's (b) eigenvalues, but the states labeled N have small admixtures of $N \pm 2$.

The spin-orbit term includes both the interaction of the electronic spin with the field produced by the rotating nuclei and "L uncoupling," where interaction with the molecular rotation causes the electronic states to have some electronic angular momentum along the axis of molecular rotation. The diagonal elements of this term are $\gamma(N+1)$ for $J = N+1$ states, $-\gamma N$ for $J = N-1$ states and zero for $J = N$ states, with $\gamma = 0.25$ GHz. These terms increase in size as N increases, but are still much smaller than the spin-spin terms for all appreciably populated states under atmospheric conditions.

1.1.3 Nuclear Symmetry Constraints

Molecules with identical nuclei have overall wave functions with definite symmetry under exchange of nuclei: those with identical boson nuclei ($^{16}O_2$ and $^{18}O_2$) must have total wave functions that are even under exchange of the nuclei and those with identical fermion nuclei ($^{17}O_2$) must be odd. Nuclei may be exchanged by an end-over-end half rotation of the entire molecule (even for even values of N) and then returning the electrons to their original positions, which uses the "g" and "$-$" symmetries of the electronic state. For the $^3\Sigma_g^-$ electronic ground state, symmetry requirements limit $^{16}O_2$ and $^{18}O_2$ to rotational states with odd values of the quantum number N.

The relative abundances of oxygen isotopes in the earth atmosphere are: ^{16}O 99.758%, ^{18}O 0.204%, and ^{17}O 0.037%, so discussion can be limited to $^{16}O_2$ (99.517% of diatomic

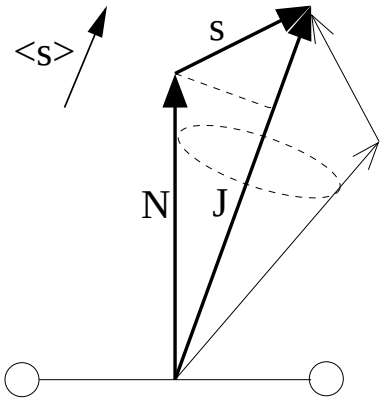

Figure 1.1: In Hund's case (b), $\boldsymbol{s}$ adds to $\boldsymbol{N}$ to give total angular momentum, $\boldsymbol{J}$. Time-averaged $\langle \boldsymbol{s} \rangle$ is the projection of $\boldsymbol{s}$ on $\boldsymbol{J}$. Oxygen eigenstates are not exactly Hund's (b), but are found by diagonalizing the Hamiltonian. The resulting eigenstates are labeled with quantum numbers of the Hund's (b) state which they most closely resemble.

oxygen,) $^{16}O^{18}O$ (0.408%) and $^{16}O^{17}O$ (0.075%.) These abundances hold throughout the parts of the atmosphere under consideration in this work because O_2 is the reservoir for oxygen atoms.

1.1.4 Zeeman Splitting

The combined spin, $\boldsymbol{s}$, of the two unpaired electrons has an associated magnetic moment, $\boldsymbol{\mu} = -g_e \mu_B \boldsymbol{s}$, where μ_B is the Bohr magneton and $g_e \approx 2.00229$ is the gyro-magnetic ratio of an electron. This magnetic moment interacts with the geomagnetic field, $\boldsymbol{\mathcal{H}}_{\rm geo}$, giving a magnetic Hamiltonian,

$$\mathrm{H}_{\rm mag} = -\boldsymbol{\mu} \cdot \boldsymbol{\mathcal{H}}_{\rm geo} \tag{1.2}$$

In O_2, the coupling between $\boldsymbol{s}$ and $\boldsymbol{N}$ is much stronger than the magnetic interaction of $\boldsymbol{s}$ with $\boldsymbol{\mathcal{H}}_{\rm geo}$. Classically, electronic spin $\boldsymbol{s}$ precesses rapidly about $\boldsymbol{J}$, so that for weaker, slower-precessing interactions we can use the time-averaged value of $\boldsymbol{s}$, which is its projection on $\boldsymbol{J}$. The time-averaged magnetic moment, $< \boldsymbol{\mu} >$, associated with the time-averaged electronic spin, $< \boldsymbol{s} >$ drags $\boldsymbol{J}$ around $\boldsymbol{\mathcal{H}}_{\rm geo}$. Thus, to get the magnitude of $\boldsymbol{\mu} \cdot \boldsymbol{\mathcal{H}}_{\rm geo}$ we first project $\boldsymbol{\mu}$ onto the direction of $\boldsymbol{J}$, $\hat{\boldsymbol{J}}$, and then $\hat{\boldsymbol{J}}$ onto $\boldsymbol{\mathcal{H}}_{\rm geo}$.

$$\begin{aligned} \mathrm{H}_{\rm mag} &= g_e \mu_B (\boldsymbol{s} \cdot \hat{\boldsymbol{J}})(\hat{\boldsymbol{J}} \cdot \boldsymbol{\mathcal{H}}_{\rm geo}) \,, \\ &= g_e \mu_B \frac{(\boldsymbol{s} \cdot \boldsymbol{J})(\boldsymbol{J} \cdot \boldsymbol{\mathcal{H}}_{\rm geo})}{\boldsymbol{J}^2} \,, \end{aligned}$$

but $\boldsymbol{N}^2 = \boldsymbol{J}^2 + \boldsymbol{s}^2 - 2\boldsymbol{J} \cdot \boldsymbol{s}$, so

$$\mathrm{H}_{\rm mag} = g_e \mu_B \frac{\boldsymbol{J}^2 + \boldsymbol{s}^2 - \boldsymbol{N}^2}{2\boldsymbol{J}^2} \boldsymbol{J} \cdot \boldsymbol{\mathcal{H}}_{\rm geo} \,,$$

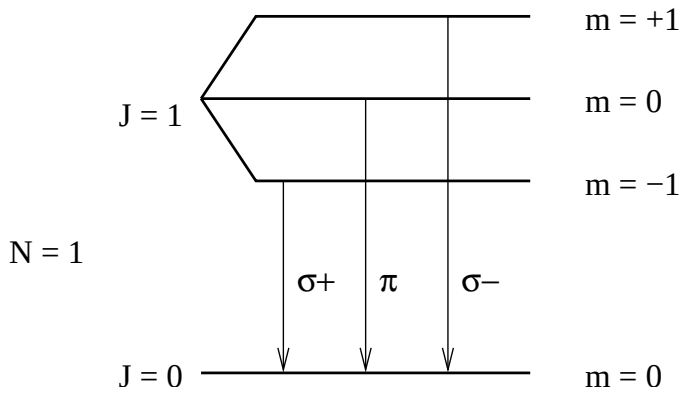

Figure 1.2: The 1- line has three Zeeman components. This cartoon is very much not to scale as all three transitions are approximately 118.7506 GHz, with Zeeman splitting in typical geomagnetic fields of order 1 MHz.

Zeeman Frequency Shifts, $\Delta\nu$			
	N_+ lines	N_- lines	1_- case
σ_+	$-\kappa$ H $\frac{m(N-1)+N}{N(N+1)}$	κ H $\frac{m(N+2)+N+1}{N(N+1)}$	$\frac{1}{2}\kappa H$
π	$-\kappa$ H $\frac{m(N-1)}{N(N+1)}$	κ H $\frac{m(N+2)}{N(N+1)}$	0
σ_-	$-\kappa$ H $\frac{m(N-1)-N}{N(N+1)}$	κ H $\frac{m(N+2)-N-1}{N(N+1)}$	$-\frac{1}{2}\kappa H$
$\kappa = 2.8024\,\mathrm{MHz/gauss}$			

Table 1.1: O_2 Zeeman component line frequency shifts relative to the zero field position. The quantum number, m, is of the upper state, and the constant κ is $g_e\mu_B$.

and for Hund's case (b) eigenstates, diagonal matrix elements,

$$\mathrm{H_{mag}} = \frac{J(J+1)+s(s+1)-N(N+1)}{2J(J+1)} g_e m \mu_B |\boldsymbol{\mathcal{H}}_{\mathrm{geo}}| \; . \tag{1.3}$$

While Equation 1.3 is exact for pure Hund's (b) eigenstates, it must be adjusted to account for small admixtures of states with rotational quantum number N and $N \pm 2$, which are required for diagonalization of the Hamiltonian. [8]. This may be accounted for by tabulating adjusted g_e values for each state. These values are tabulated in the JPL Spectral Line Catalog. [9] The g_e for the 118-GHz line is the free-space value, so no correction is needed in this case. This sort of correction is discussed by Sandor and Clancy in reference to the 239-GHz $^{18}O^{16}O$ line.[13]

Zeeman Fractional Intensities, $\xi(m, \Delta m)$			
	N_+ lines	N_- lines	1_- case
$\Delta m = +1 \leftrightarrow \sigma_+$	$\frac{3(N+m+1)(N+m+2)}{4(N+1)(2N+1)(2N+3)}$	$\frac{3(N-m)(N-m-1)}{4N(2N+1)(2N-1)}$	$\frac{1}{2}$
$\Delta m = 0 \leftrightarrow \pi$	$\frac{3[(N+1)^2-m^2]}{(N+1)(2N+1)(2N+3)}$	$\frac{3(N^2-m^2)}{N(2n+1)(2N-1)}$	1
$\Delta m = -1 \leftrightarrow \sigma_-$	$\frac{3(N-m+1)(N-m+2)}{4(N+1)(2N+1)(2N+3)}$	$\frac{3(N+m)(N+m-1)}{4N(2N+1)(2N-1)}$	$\frac{1}{2}$

Table 1.2: O_2 Zeeman component fractional intensities. These values are normalized so that the zero-field case reduces to the scalar equations for each diagonal element of the matrix expressions. The quantum number, m, is of the upper state.

1.2 Magnetic Dipole Transitions

1.2.1 Selection Rules

Magnetic dipole transitions obey the following selection rules:

$$|\Delta J| \leq 1 \leq J_i + J_f \tag{1.4}$$

$$|\Delta m| \leq 1, \tag{1.5}$$

$$\Delta N \in 0, \pm 2\ . \tag{1.6}$$

The second inequality in the first selection rule is included to specifically forbid transitions from $J_i = 0$ to $J_f = 0$. The third selection rule results from the fact that the magnetic dipole operator is even, and has nonzero matrix elements only between states that have the same parity. For the transitions between spin-rotational states of the ${}^3\Sigma_g^-$ ground state of ${}^{16}O_2$, the restriction due to nuclear symmetry constrains N to odd values, so the question of transitions with $\Delta N = 1$ is moot. Parity does forbid many transitions that would otherwise be present in ${}^{16}O{}^{18}O$. Figure 1.3 diagrams the lowest energy O_2 spin-rotational states, with states permitted for both ${}^{16}O{}^{18}O$ and ${}^{16}O_2$ drawn with solid lines, and those that refer only to ${}^{16}O{}^{18}O$ drawn with dashed lines. This diagram is not to scale, and does not reflect frequency shifts between the O_2 isotopic species.

Lines that are transitions between states with the same N are generally designated $N+$ or $N-$ depending upon whether ΔJ goes up or down. The MLS spectroscopy database [10] labels lines (N_{upper}, J_{upper}, N_{lower}, J_{lower}). A third notation, shown in Figure 1.3, is a 4-character line designation in the form (ΔN N_{lower} ΔJ J_{lower}) where changes ($\Delta N, \Delta J$) are labeled P, Q, R, S for $1, 0, -1, -2$ respectively. The 118-GHz line in band 1 is variously labeled (1-), 1110, or Q1R0. The 234-GHz ${}^{16}O{}^{18}O$ line in band 8 is labeled 2101 or S0Q1.

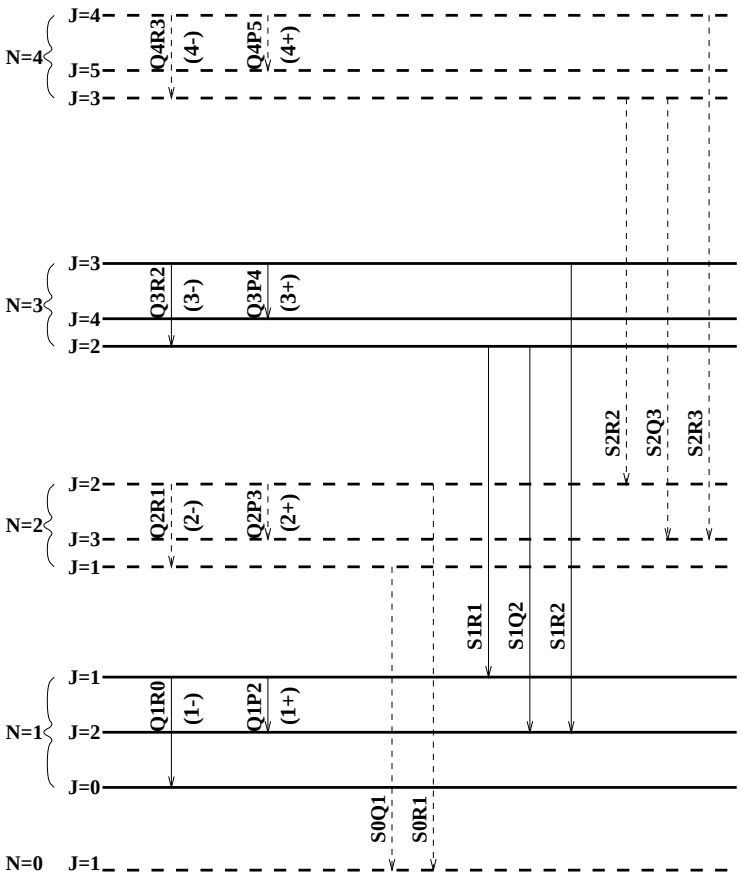

Figure 1.3: Magnetic dipole transitions within the O_2 electronic ground state. Only the solid-line, odd rotational states are permitted for $^{16}O_2$ and $^{18}O^{18}O$ in their electronic ground states, while only the dashed-line, even rotational states are permitted for $^{17}O^{17}O$. There are no such restrictions on molecules without identical nuclei. The 118-GHz line is Q1R0. The 234-GHz $^{16}O^{18}O$ line in band 8 is S0Q1.

1.3 Tensor magnetic susceptibility

The dependence of the magnetic susceptibility on the angles between an imposed geomagnetic field and the propagation polarization is what gives the radiative transfer described in this document its matrix character. The three eigenvectors of $\boldsymbol{\chi}$ link three eigen-polarizations to the three allowed Δm transitions: ± 1 and 0. The factoring of a common angular dependence for all lines in each of σ_+, π, and σ_- is a manifestation of the Wigner-Eckart theorem [6].

The magnetic susceptibility $\boldsymbol{\chi}$ is proportional to a product of matrix elements of the magnetic dipole moment operator $\boldsymbol{\mu}$

$$\chi_{ij} \propto \sum_{\alpha,\beta} \langle J_\alpha, m_\alpha | \, \mu_i \, | J_\beta, m_\beta \rangle \, \langle J_\beta, m_\beta | \, \mu_j^\dagger \, | J_\alpha, m_\alpha \rangle \tag{1.7}$$

where i, j are the spatial components of the dipole operator. The lines under consideration are the transitions, $\alpha \rightarrow \beta$. This object is a tensor, so if we can determine it in any basis, we can express it in any other basis via a unitary transformation. In this discussion, we will consider the polarization of radiation to be the direction of its magnetic field vector, $\hat{H}_{\rm RF}$. We will consider a polarization basis (i, j) where the $\hat{z}$ direction is that of the geomagnetic field. Linearly polarized radiation with its magnetic field aligned in the $\hat{z}$ direction (along $\boldsymbol{\mathcal{H}}_{\rm geo}$) couples only to π transitions. In the $x - y$ polarization plane, (which has its $\hat{H}_{\rm RF}$ perpendicular to $\boldsymbol{\mathcal{H}}_{\rm geo}$,) left and right circular polarizations couple only to σ_+ and σ_- transitions, respectively. In a basis of these three polarizations, χ_{ij} is diagonal.

$$\boldsymbol{\chi}''' = \begin{bmatrix} \chi_+ & 0 & 0 \\ 0 & \chi_- & 0 \\ 0 & 0 & \chi_0 \end{bmatrix} \tag{1.8}$$

We can transform this expression to a linear polarization basis $\{\hat{x},\, \hat{y},\, \hat{z}\}$ with the unitary transformation

$$\begin{aligned} \boldsymbol{\chi}'' &= \boldsymbol{R_c} \boldsymbol{\chi} \boldsymbol{R_c}^\dagger \\ &= \begin{bmatrix} (\chi_+ + \chi_-)/2 & -i(\chi_+ - \chi_-)/2 & 0 \\ i(\chi_+ - \chi_-)/2 & (\chi_+ + \chi_-)/2 & 0 \\ 0 & 0 & \chi_0 \end{bmatrix} \end{aligned} \tag{1.9}$$

where

$$\boldsymbol{R_c} = \begin{bmatrix} \frac{1}{\sqrt{2}} & \frac{i}{\sqrt{2}} & 0 \\ \frac{i}{\sqrt{2}} & \frac{1}{\sqrt{2}} & 0 \\ 0 & 0 & 1 \end{bmatrix}$$

Rotation by an "elevation" angle, θ, about the $\hat{x}$ axis moves the direction of propagation away from the geomagnetic field direction.

$$R_\theta = \begin{bmatrix} 1 & 0 & 0 \\ 0 & \cos\theta & \sin\theta \\ 0 & -\sin\theta & \cos\theta \end{bmatrix} \tag{1.10}$$

$$\boldsymbol{\chi}' = R_\theta \boldsymbol{\chi}'' R_\theta^\dagger \tag{1.11}$$

Subsequent rotation by an "azimuth" angle, ϕ, about the $\hat{z}$ axis (line of sight) permits the field of view to be arbitrarily oriented relative to the geomagnetic field direction.

$$R_\phi = \begin{bmatrix} \cos\phi & \sin\phi & 0 \\ -\sin\phi & \cos\phi & 0 \\ 0 & 0 & 1 \end{bmatrix} \tag{1.12}$$

$$\boldsymbol{\chi} = R_\phi R_\theta \boldsymbol{\chi}'' R_\theta^\dagger R_\phi^\dagger \tag{1.13}$$

Under the assumption that the waves are transverse (we are neglecting H_z) we drop the third row and column of this 3×3 tensor and get the result in Lenoir. The frame of reference which will be used in discussions of EOS-MLS in Chapter 3 is the Instrument Field of View Polarized Pointing (IFOVPP) frame where $\hat{z}$ is in the direction of propagation and $\hat{x}$ is in the direction of In the IFOVPP, $\boldsymbol{\chi} = \chi_+ \boldsymbol{\rho}_+ + \chi_- \boldsymbol{\rho}_- + \chi_0 \boldsymbol{\rho}_0$ where

$$\begin{aligned} \boldsymbol{\rho}_{\pm 1} &= \begin{bmatrix} \cos^2\phi + \sin^2\phi\cos^2\theta & -\sin\phi\cos\phi\sin^2\theta \mp \imath\cos\theta \\ -\sin\phi\cos\phi\sin^2\theta \pm \imath\cos\theta & \sin^2\phi + \cos^2\phi\cos^2\theta \end{bmatrix}, \\ \boldsymbol{\rho}_0 &= \begin{bmatrix} \sin^2\phi\sin^2\theta & \sin\phi\cos\phi\sin^2\theta \\ \sin\phi\cos\phi\sin^2\theta & \cos^2\phi\sin^2\theta \end{bmatrix}. \end{aligned} \tag{1.14}$$

As R_ϕ involves only the $\vec{\boldsymbol{x}}$ and $\vec{\boldsymbol{y}}$ directions, the ϕ rotation can be done either before or after the projection into two dimensions.

Chapter 2

Polarized Radiative Transfer

Absorption and emission by resolved Zeeman components depends upon the orientation of the geomagnetic field relative to the directions of radiation propagation and polarization. The magnetic susceptibility matrix has off-diagonal elements that mix polarizations as the wave propagates, so that the equations of radiative transfer for different polarizations are coupled. This is an example of Faraday rotation of propagating radiation by a non-ionized atmospheric constituent. Lenoir [6][7] developed methods of doing radiative transfer calculations with 2x2 coherence matrix tensors, and applied this theory to the case of Zeeman-split microwave oxygen lines. Rosenkranz and Staelin [12] and Stogryn [15] advanced this work.

2.1 Field Equations

This section follows Lenoir to derive the radiative transfer equation for a medium with a slightly anisotropic magnetic susceptibility. In this section, 3-dimensional vectors such as fields in the Maxwell equations are denoted $\underline{\mathsf{E}}$, 3x3 matrices are denoted $\underline{\underline{\chi}}$. When we project equations into x-y 2-dimensional space, we will denote vectors as $\vec{\mathsf{E}}$ and matrices as $\boldsymbol{\chi}$.

The source-free (no free charge or currents) Maxwell Equations for a harmonic field, assuming $e^{-i\omega t}$ time dependence are

$$\begin{aligned}
\underline{\nabla} \times \underline{\mathsf{E}}(\underline{\mathsf{r}},\omega) &= i\frac{\omega}{c}\underline{\mathsf{B}}(\underline{\mathsf{r}},\omega) \\
\underline{\nabla} \times \underline{\mathsf{H}}(\underline{\mathsf{r}},\omega) &= -i\frac{\omega}{c}\underline{\mathsf{D}}(\underline{\mathsf{r}},\omega) \\
\underline{\nabla} \cdot \underline{\mathsf{B}}(\underline{\mathsf{r}},\omega) &= 0 \\
\underline{\nabla} \cdot \underline{\mathsf{D}}(\underline{\mathsf{r}},\omega) &= 0.
\end{aligned} \tag{2.1}$$

In the spectral vicinity of the Zeeman-split oxygen microwave spectral lines, the dielectric constant is that of free space, $\epsilon = 1$, but there is a tensor magnetic susceptibility, $\underline{\underline{\chi}}$,

$$\begin{aligned}
\underline{\mathsf{D}}(\underline{\mathsf{r}},\omega) &= \underline{\mathsf{E}}(\underline{\mathsf{r}},\omega) \\
\underline{\mathsf{B}}(\underline{\mathsf{r}},\omega) &= \underline{\underline{\mu}}(\omega)\underline{\mathsf{H}}(\underline{\mathsf{r}},\omega) \\
\underline{\underline{\mu}}(\omega) &= \underline{\underline{1}} + \underline{\underline{\chi}}(\omega).
\end{aligned} \tag{2.2}$$

For the cases under consideration here, all components of $\underline{\underline{\chi}}$ are small:

$$\chi_{ij} \ll 1. \tag{2.3}$$

As usual, we take the curl of the second Maxwell equation and combine it with the first to get the wave equation for $\underline{\mathsf{H}}$.

$$\underline{\nabla}^2\underline{\mathsf{H}}(\underline{\mathsf{r}},\omega) + k_0^2[\underline{\underline{1}} + \underline{\underline{\chi}}(\omega)]\underline{\mathsf{H}}(\underline{\mathsf{r}},\omega) - \underline{\nabla}[\underline{\nabla}\cdot\underline{\mathsf{H}}(\underline{\mathsf{r}},\omega)] = 0. \tag{2.4}$$

Here, $k_0 = \frac{\omega}{c}$. Now, assume a plane-wave solution with fields depending only upon z, the direction of propagation.

$$\frac{\partial^2}{\partial z^2}[\underline{\mathsf{H}}(z,\omega) - H_z(z,\omega)\hat{\boldsymbol{z}}] + k_0^2[\underline{\underline{1}} + \underline{\underline{\chi}}(\omega)]\underline{\mathsf{H}}(z,\omega) = 0\ . \tag{2.5}$$

The z-component of Equation 2.5 is

$$\mathsf{H}_z(z,\omega) = \frac{-\chi_{zx}(\omega)}{1+\chi_{zz}(\omega)}\mathsf{H}_x(z,\omega) - \frac{\chi_{zy}(\omega)}{1+\chi_{zz}(\omega)}\mathsf{H}_y(z,\omega), \tag{2.6}$$

and since $\chi_{ij} \ll 1$,

$$|\mathsf{H}_z| \ll |\mathsf{H}_x|, |\mathsf{H}_y|. \tag{2.7}$$

Since ϵ is scalar, $\underline{\mathsf{E}}$ is exactly transverse ($E_z = 0$). If H_z is negligible, we can drop the $\hat{z}$ direction from our equations altogether. In the xy space, the wave equation may be expressed in terms of a propagation matrix, $\boldsymbol{G}$,

$$\begin{aligned} \frac{\partial^2}{\partial z^2}\vec{\mathsf{H}}(z,\omega) - \boldsymbol{G}^2\vec{\mathsf{H}}(z,\omega) &= 0\ , \qquad (2.8) \\ \text{where} & \\ \boldsymbol{G}^2 &= -k_0^2[\mathbf{1} + \boldsymbol{\chi}(\omega)], \\ \boldsymbol{G} &\approx -ik_0[\mathbf{1} + \frac{\boldsymbol{\chi}(\omega)}{2}]. \qquad (2.9) \end{aligned}$$

Here, as in Stogryn, we have chosen the negative square-root to go with the $e^{-i\omega t}$ time dependence.

Lenoir says that the validity of the neglect of fields along the direction of propagation requires

$$\Re[\chi_{xz}\chi_{zx} + \frac{1}{2}\chi_{xx}^2]z_{\max} \ll 1, \tag{2.10}$$

where $z_{\max}$ is is the total distance along the propagation direction, which I assume to be scaled in units of wavelength. He says this should not be of concern for radiative transfer in the upper part of the earth's atmosphere, except for extraordinarily long pathlength. The validity of this approximation should be checked for our long limb-viewing geometry.

Equation 2.8, the wave equation for propagation through a uniform medium, has a general solution

$$\vec{\mathsf{H}}(z,\omega) = \exp[-\boldsymbol{G}(\omega)z]\vec{\mathsf{H}}(0,\omega). \tag{2.11}$$

If the medium is not uniform, but is stratified along the direction of propagation, propagation matrices, $\boldsymbol{G}(z,\omega)$, for different values of z will not generally commute. The matrix exponentials must be applied, in order, from the left-hand side for each uniform slab.

$$\vec{\mathsf{H}}(z_n,\omega) = \exp[-\boldsymbol{G}(z_n,\omega)dz_n]\ldots\exp[-\boldsymbol{G}(z_2,\omega)dz_2]\exp[-\boldsymbol{G}(z_1,\omega)dz_1]\vec{\mathsf{H}}(0,\omega). \tag{2.12}$$

2.2 Two-Dimensional Field Equations

Given the assumption that the fields $\vec{\mathsf{E}}(z,\omega)$ and $\vec{\mathsf{H}}(z,\omega)$ are in the 2-dimensional x-y space, the curl operator becomes

$$\underline{\nabla}\times \rightarrow \frac{\partial}{\partial z}\boldsymbol{U}^{-1} \tag{2.13}$$

where $\boldsymbol{U}$ is a rotation by 90°,

$$\begin{aligned}\boldsymbol{U} &= \begin{bmatrix} 0 & 1 \\ -1 & 0 \end{bmatrix} \\ \boldsymbol{U}^{-1} &= \boldsymbol{U}^T = -\boldsymbol{U}\,.\end{aligned} \tag{2.14}$$

The first two Maxwell equations involving curl can be rewritten

$$\frac{\partial \vec{\mathsf{E}}_p}{\partial z} = -\frac{i}{k_0}\boldsymbol{G}^2\vec{\mathsf{H}}\,, \tag{2.15}$$

$$\frac{\partial \vec{\mathsf{H}}}{\partial z} = ik_0\vec{\mathsf{E}}_p\,, \tag{2.16}$$

where

$$\begin{aligned}\vec{\mathsf{E}}_p &\equiv \begin{bmatrix} -E_y \\ E_x \end{bmatrix} = \boldsymbol{U}^{-1}\begin{bmatrix} E_x \\ E_y \end{bmatrix}\,, \\ \vec{\mathsf{H}} &\equiv \begin{bmatrix} H_x \\ H_y \end{bmatrix}\,, \\ \boldsymbol{G} &\equiv \begin{bmatrix} G_{xx} & G_{xy} \\ G_{yx} & G_{yy} \end{bmatrix} = -ik_0(\mathbf{1} + \frac{\boldsymbol{\chi}}{2})\,.\end{aligned}$$

Plugging our form for $\vec{\mathsf{H}}$ from Equation 2.11 into Equation 2.16 and rearranging a bit we get an equation relating $\vec{\mathsf{E}}_p$ and $\vec{\mathsf{H}}$,

$$\vec{\mathsf{E}}_p = \frac{i}{k_0}\boldsymbol{G}\vec{\mathsf{H}}\,. \tag{2.17}$$

2.3 Coherence Matrices

Lenoir defines the complex power-spectrum coherence matrix

$$\begin{aligned}\boldsymbol{I}(\omega) &= \left\langle \underline{\mathsf{E}}_p(\omega)\underline{\mathsf{H}}^\dagger(\omega)\right\rangle \\ &= \begin{bmatrix} \langle -E_yH_x^*\rangle & \left\langle -E_yH_y^*\right\rangle \\ \langle E_xH_x^*\rangle & \left\langle E_xH_y^*\right\rangle \end{bmatrix}\end{aligned} \tag{2.18}$$

where $\langle\ \rangle$ denotes ensemble averaging. The diagonals of the coherence matrix are proportional to the power propagated in two polarizations, the first has $\underline{\mathsf{H}}$ in the $\hat{x}$ direction and the second

has $\underline{\mathsf{H}}$ in the $\hat{y}$ direction. The sum of these elements is proportional to the magnitude of the Poynting vector, which is power propagating in the $\hat{z}$ direction. [4]

$$\begin{aligned}\underline{\mathsf{S}} &= \frac{c}{8\pi}(\underline{\mathsf{E}} \times \underline{\mathsf{H}}^*) \\ &= \frac{c}{8\pi}(E_x H_y^* - E_y H_x^*)\hat{z}\end{aligned} \tag{2.19}$$

The off-diagonal terms give information about the coherence between the two polarizations. The equations could be recast in any polarization basis (for example, left and right circular) by applying the appropriate unitary transformation, but discussion here will assume a basis of crossed linear polarizations since this leads most naturally to a discussion of the MLS antenna polarizations.

Stogryn [15] defines his power spectrum coherence matrix $\boldsymbol{I}_{\text{Stogryn}}$ to be $U\boldsymbol{I}_{\text{Lenoir}}U^\dagger$, which is proportional to the more standard definition of the coherence matrix, $\boldsymbol{J}$.

$$\boldsymbol{J} = \begin{bmatrix}\langle E_x E_x^* \rangle & \langle E_x E_y^* \rangle \\ \langle E_y E_x^* \rangle & \langle E_y E_y^* \rangle\end{bmatrix} \tag{2.20}$$

The coherence matrix, $\boldsymbol{J}$, is manifestly Hermitian. It has real, positive eigenvalues. Its diagonal elements are proportional to the power propagated in each of the two polarizations, and the off-diagonal terms give the correlation between them. This matrix contains the same information as the more-familiar Stokes vector,

$$\boldsymbol{S} = \begin{bmatrix} J_{xx} + J_{yy} \\ J_{xx} - J_{yy} \\ J_{xy} + J_{yx} \\ i(J_{xy} - J_{yx}) \end{bmatrix} . \tag{2.21}$$

The form of $\boldsymbol{I}$ which we will use in this work is based upon Lenoir's definition, and has elements,

$$\boldsymbol{I} = \begin{bmatrix} I_\parallel & I_| + \imath I_\circ \\ I_| - \imath I_\circ & I_\perp \end{bmatrix} , \tag{2.22}$$

where $I_\parallel$ and $I_\perp$ are radiated power (scalar brightness temperatures) in the two linear polarizations and $I_\circ$ and $I_|$ are their circular and linear coherences.

2.4 Tensor Radiative Transfer

For radiative transfer, we are interested in how the quantity $\boldsymbol{I}$ changes along the direction of propagation. From this point forward, we will refer to this direction as $\hat{s}$ rather than $\hat{z}$.

$$\frac{\mathrm{d}\boldsymbol{I}}{\mathrm{d}s} = \left\langle \frac{\mathrm{d}\vec{\mathsf{E}}_p}{\mathrm{d}s}\vec{\mathsf{H}}^\dagger \right\rangle + \left\langle \vec{\mathsf{E}}_p \frac{\mathrm{d}\vec{\mathsf{H}}^\dagger}{\mathrm{d}s} \right\rangle .$$

Substituting from Equation 2.15 and the complex conjugate of Equation 2.16 gives

$$\frac{\mathrm{d}\boldsymbol{I}}{\mathrm{d}s} = -\frac{i}{k_0}\left\langle \boldsymbol{G}^2 \vec{\mathsf{H}}\vec{\mathsf{H}}^\dagger \right\rangle - ik_0 \left\langle \vec{\mathsf{E}}_p \vec{\mathsf{E}}_p^\dagger \right\rangle . \tag{2.23}$$

Substituting Equation 2.17, $\vec{\mathsf{E}}_p = \frac{i}{k_0}\boldsymbol{G}\vec{\mathsf{H}}$, and its complex conjugate, we get

$$\begin{aligned}\frac{\mathrm{d}\boldsymbol{I}}{\mathrm{d}s} &= -\boldsymbol{G}\vec{\mathsf{E}}_p\vec{\mathsf{H}}^\dagger - \vec{\mathsf{E}}_p\vec{\mathsf{H}}^\dagger\boldsymbol{G}^\dagger \\ &= -\boldsymbol{G}\boldsymbol{I} - \boldsymbol{I}\boldsymbol{G}^\dagger \\ &= \left(\frac{ik_0}{2}\boldsymbol{\chi}\right)\boldsymbol{I} + \boldsymbol{I}\left(\frac{ik_0}{2}\boldsymbol{\chi}\right)^\dagger \ . \end{aligned} \tag{2.24}$$

In the last equality, the part of $\boldsymbol{G}$ corresponding to the free propagator, $ik_0\mathbf{1}$, has canceled in the two terms. This part of the phase has no impact on power transmission.

The preceding semi-classical derivation gives us a polarized equation of radiative transfer which lacks spontaneous emission. If we consider the unpolarized case, $\boldsymbol{\chi} = \chi_u\mathbf{1}$, each of the diagonals will give the scalar radiative transfer equation with

$$\frac{\mathrm{d}\boldsymbol{I}}{\mathrm{d}s} = -k_0\,\mathrm{Im}\,(\chi_u)\boldsymbol{I}\ . \tag{2.25}$$

Positive, imaginary parts of χ give absorption. We can handle isotropic spontaneous emission by replacing $\boldsymbol{I}$ on the right-hand side of Equation 2.25 with $(\boldsymbol{I} - B\mathbf{1})$, where B is the scalar Planck source function for thermal radiation in equilibrium at temperature T,

$$B(T_{air}) = \frac{h\nu}{k(\exp\{\frac{h\nu}{kT_{air}}\} - 1)}\,, \tag{2.26}$$

This brings us, finally, to the equation for polarized radiative transfer in a slightly anisotropic medium,

$$\frac{\mathrm{d}\boldsymbol{I}}{\mathrm{d}s} = \boldsymbol{G}\,(B - \boldsymbol{I}) + (B - \boldsymbol{I})\,\boldsymbol{G}^\dagger\ . \tag{2.27}$$

This equation is the basis for our model of transmission near the Zeeman-split oxygen lines. The solution for radiative transfer through a uniform slab of atmosphere of thickness z may be written

$$\boldsymbol{I}(z) = B + \exp(-\boldsymbol{G}z)(\boldsymbol{I}(0) - B)\exp(-\boldsymbol{G}z)^\dagger. \tag{2.28}$$

Here, B, $\boldsymbol{G}$ and z are properties of the uniform *layer*, while $\boldsymbol{I}(z)$ and $\boldsymbol{I}(0)$ are intensities at the layer boundaries. Matrix exponentiation has its usual definition as a power series.

$$\exp\,(\boldsymbol{A}) = \mathbf{1} + \boldsymbol{A} + \frac{1}{2}\boldsymbol{A}\boldsymbol{A} + \ldots \tag{2.29}$$

Algorithms for the evaluation of matrix exponentials and their derivatives are given in Appendix A.

For multiple layers that have different $\boldsymbol{G}$, the matrix exponentials must be time-ordered. A power series of integrals over the path must have the integral broken into sums at ordered times, which are then sorted in all of the products so that the earlier times are to the right. We do this ordering, explicitly, by ordering matrix multiplication with discrete expressions.

Here, we adopt the indexing scheme used in the scalar code, in which the first layer boundary is the top of the atmosphere closest to the observer, the tangent point is labeled t when discussing the near side of the tangent point and $2N-t+1$ when discussing the far side of the tangent point, and the top of the atmosphere beyond the tangent point is $2N$. There

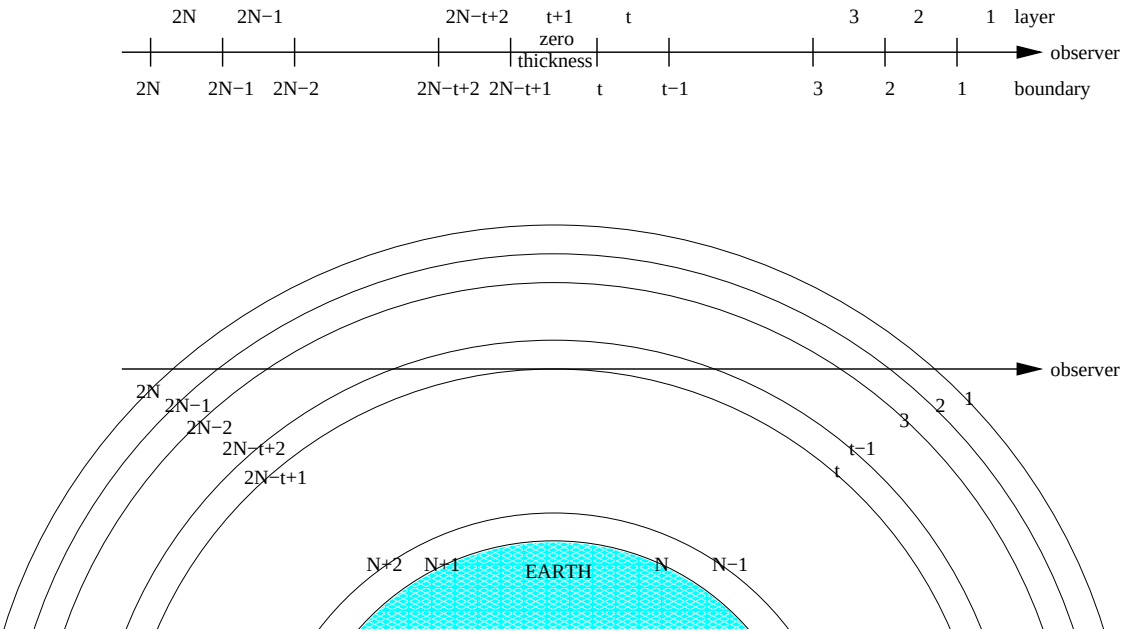

Figure 2.1: This layer indexing scheme is consistent with that used in the scalar model. The lower figure labels only the layer boundaries. The upper also labels the layers, including a zero-thickness layer at the tangent point. Each pointing is labeled by its tangent index, t.

are $N-1$ layers between the top of the atmosphere and the surface of the earth, but the line-of-sight tangent path only comes down to layer t. This indexing is shown in Figure 2.1. The jth layer is on the side of the jth layer boundary closest to the observer. Layer 1 is between layer boundary 1 and the observer and has $\boldsymbol{G} = 0$.

We define the field layer transmittance for the jth layer:

$$\boldsymbol{E}_j = \exp\left(-\int_{s_j}^{s_{j-1}} \boldsymbol{G}(s')\,ds'\right) ,$$

with the special cases,

$$\begin{aligned} \boldsymbol{E}_1 &= \mathbf{1} , \\ \boldsymbol{E}_{t+1} &= \boldsymbol{\Upsilon}_f , \end{aligned} \tag{2.30}$$

The layer boundary indices t and $2N-t+1$ both refer to the tangent point, and the layer field transmittance for the zero-thickness layer between them, $\boldsymbol{E}_{t+1}$, is defined to be the Earth field reflectivity,$\boldsymbol{\Upsilon}_f$, for instances where the path intersects the Earth, and $\mathbf{1}$ otherwise. We will ignore polarization effects in the reflection and use the identity matrix times the square-root of the scalar model's "power" reflectivity as the "field" reflectivity.

$$\boldsymbol{\Upsilon}_f = \sqrt{\Upsilon}\mathbf{1} \tag{2.31}$$

Layers are assumed to be thin enough that $\boldsymbol{G}_j(s)$ commutes with itself within each layer.

Now we can recast Equation 2.28 to give the expression for radiative transfer through layer $j+1$ as

$$\boldsymbol{I}_j = \left(\frac{B_{j+1}+B_j}{2}\right)\left(1-\boldsymbol{E}_{j+1}\boldsymbol{E}_{j+1}^\dagger\right)+\boldsymbol{E}_{j+1}\boldsymbol{I}_{j+1}\boldsymbol{E}_{j+1}^\dagger\,, \tag{2.32}$$

where B_j is the source function for the temperature of the jth slab boundary. If we apply this recursion relation a few times we can see the pattern emerge:

$$\begin{aligned}\boldsymbol{I}_1 = &\left(\frac{B_1+B_2}{2}\right)\left(\boldsymbol{E}_1\boldsymbol{E}_1^\dagger-\boldsymbol{E}_1\boldsymbol{E}_2\boldsymbol{E}_2^\dagger\boldsymbol{E}_1^\dagger\right)\\ &+\left(\frac{B_2+B_3}{2}\right)\left(\boldsymbol{E}_1\boldsymbol{E}_2\boldsymbol{E}_2^\dagger\boldsymbol{E}_1^\dagger-\boldsymbol{E}_1\boldsymbol{E}_2\boldsymbol{E}_3\boldsymbol{E}_3^\dagger\boldsymbol{E}_2^\dagger\boldsymbol{E}_1^\dagger\right)\\ &+\left(\frac{B_3+B_4}{2}\right)\left(\boldsymbol{E}_1\boldsymbol{E}_2\boldsymbol{E}_3\boldsymbol{E}_3^\dagger\boldsymbol{E}_2^\dagger\boldsymbol{E}_1^\dagger-\boldsymbol{E}_1\boldsymbol{E}_2\boldsymbol{E}_3\boldsymbol{E}_4\boldsymbol{E}_4^\dagger\boldsymbol{E}_3^\dagger\boldsymbol{E}_2^\dagger\boldsymbol{E}_1^\dagger\right)\\ &+\boldsymbol{E}_1\boldsymbol{E}_2\boldsymbol{E}_3\boldsymbol{E}_4\boldsymbol{I}_4\boldsymbol{E}_4^\dagger\boldsymbol{E}_3^\dagger\boldsymbol{E}_2^\dagger\boldsymbol{E}_1^\dagger\,.\end{aligned} \tag{2.33}$$

We define product matrices, $\boldsymbol{P}_j$, which can be thought of as the time-ordered exponential of the integral of $\boldsymbol{G}$ from the far side of the jth layer to the observer (beyond boundary 1.)

$$\begin{aligned}\boldsymbol{P}_1 &= \boldsymbol{E}_1 = \mathbf{1}\\ \boldsymbol{P}_2 &= \boldsymbol{P}_1\,\boldsymbol{E}_2\\ \boldsymbol{P}_3 &= \boldsymbol{P}_2\,\boldsymbol{E}_3\\ &\vdots\\ \boldsymbol{P}_{i+1} &= \boldsymbol{P}_i\,\boldsymbol{E}_{i+1}\\ &\vdots\\ \boldsymbol{P}_t &= \boldsymbol{P}_{t-1}\,\boldsymbol{E}_t\\ \boldsymbol{P}_{2N-t+1} &= \boldsymbol{P}_t\,\boldsymbol{\Upsilon}_f\\ \boldsymbol{P}_{2N-t+2} &= \boldsymbol{P}_{2N-t+1}\,\boldsymbol{E}_{2N-t+1}\\ &\vdots\\ \boldsymbol{P}_{2N} &= \boldsymbol{P}_{2N-1}\,\boldsymbol{E}_{2N}\end{aligned} \tag{2.34}$$

We can write the radiance emergent above the first layer:

$$\begin{aligned}\boldsymbol{I}_1 = &\sum_{i=1}^{t}(\boldsymbol{P}_i\,\boldsymbol{P}_i^\dagger-\boldsymbol{P}_{i+1}\,\boldsymbol{P}_{i+1}^\dagger)\left(\frac{B_i+B_{i+1}}{2}\right)\\ &+\sum_{i=2N-t+1}^{2N-1}(\boldsymbol{P}_i\,\boldsymbol{P}_i^\dagger-\boldsymbol{P}_{i+1}\,\boldsymbol{P}_{i+1}^\dagger)\left(\frac{B_i+B_{i+1}}{2}\right)\\ &+\boldsymbol{P}_{2N}\,\boldsymbol{I}_{2N+1}\,\boldsymbol{P}_{2N}^\dagger\,.\end{aligned} \tag{2.35}$$

The terms in the summations of Equation 2.35 are radiative transfer through layer $i+1$ for each index, i. The first sum includes the zero-thickness layer at the tangent point, which

contributes ${\Upsilon_f}^2$ of the incoming radiance and $(1 - {\Upsilon_f}^2)$ times the earth surface temperature if the ray intersects the earth. The 2D ray-tracing in the "metrics" routines shared with the scalar model determine the direction of the incoming ray, assuming specular reflection, in the event that a ray intersects the earth.

We can rewrite this expression as a single sum including the layers below the tangent layer if we make certain that $\boldsymbol{E} = 1$ for all of these extra layers, so that they do not contribute.

$$\begin{aligned} \boldsymbol{E}_{t+1} &= \boldsymbol{\Upsilon}_f \\ \boldsymbol{E}_{t+2} \ldots \boldsymbol{E}_{2N-t+1} &= \mathbf{1} \\ \boldsymbol{P}_{t+1} \ldots \boldsymbol{P}_{2N-t+1} &= \mathbf{1} \end{aligned} \tag{2.36}$$

These extra, non-contributing terms are not included in the production code, but will be included here just to make the handling of the tangent more transparent.

For a limb-sounding geometry, where layer $2N$ is the top layer of the atmosphere away from the observer, $\boldsymbol{I}_{2N+1}$ is the unpolarized cosmic background radiance, T_{cosmic}, a multiple of the identity matrix that can be pulled out of its product-matrix sandwich. This permits the radiative transfer equation to be written in terms of a transmittance matrix,

$$\boldsymbol{\mathcal{T}}_i \equiv \boldsymbol{P}_i \, \boldsymbol{P}_i^\dagger \, . \tag{2.37}$$

Gathering terms for each $\boldsymbol{\mathcal{T}}_i$, we get

$$\boldsymbol{I}_1 = \sum_{i=1}^{2N} \boldsymbol{\mathcal{T}}_i \, \Delta B_i \tag{2.38}$$

where

$$\begin{aligned} \Delta B_i &= \frac{B_{i+1} - B_{i-1}}{2} \, , \\ \Delta B_1 &= \frac{B_1 + B_2}{2} \, , \\ \Delta B_{2N} &= T_{cosmic} \mathbf{1} - \frac{B_{2N} + B_{2N-1}}{2} \, . \end{aligned}$$

To handle the jump at the tangent point,

$$\begin{aligned} \Delta B_t &= \frac{B_t - B_{t-1}}{2} \\ \Delta B_{2N-t+1} &= \frac{B_{2N-t+2} - B_t}{2} \end{aligned}$$

and skip elements in the sum with indices i=$(t+1) \ldots (2N-t)$.

$\boldsymbol{\mathcal{T}}_i$ is analogous to the scalar transmittance from the i*th* layer boundary to the top of the atmosphere. It is manifestly Hermitian, and may be thought of as a sandwich of $\boldsymbol{E}_i$ matrices

with the earliest times (largest indices) in the center of the sandwich. Here, all indices refer to layer boundaries closest to the observer— the side from which radiation emerges from the slab.

Since radiative transfer is now cast in terms of $\boldsymbol{\mathcal{T}}_i$, which is "power" transmittance, it is no longer necessary to carry the free-propagator term, $-ik_0\mathbf{1}$, in $\boldsymbol{G}$. Exponentials of these terms can be factored out of each $\boldsymbol{E}_i$, since the identity matrix, $\mathbf{1}$ commutes with anything. For each $\boldsymbol{E}_i$ in a $\boldsymbol{\mathcal{T}}$, there is a corresponding $\boldsymbol{E}_i^\dagger$ to cancel this phase term. From this point forward, we replace Equation 2.9 with

$$\boldsymbol{G} = -ik_0\frac{\boldsymbol{\chi}(\omega)}{2} \tag{2.39}$$

This same argument applies to the real parts of χ for unpolarized molecules. The contributions of unpolarized molecules will be added to $\boldsymbol{G}$ as multiples of the identity matrix, so their dispersive parts may be factored out of $\boldsymbol{\mathcal{T}}$ and canceled. We should be able to use complex lineshapes or real lineshapes for unpolarized species and get the same results.

Chapter 3

Radiance Calculation for EOS-MLS

This chapter describes the single-frequency, ray-pointing polarized radiative transfer calculation used to model EOS-MLS radiances, and their derivatives with respect to state vector elements near the 118-GHz oxygen line center. The goal is a drop-in polarized radiative module that can use the infrastructure provided by the scalar forward model, as described in the MLS Forward Model ATBD [10].

Much of the mechanics of setting up the magnetic forward model calculation is identical to what was done in the EOS-MLS Forward Model ATBD and will not be duplicated here. This includes

- Earth Figure Ellipse
- 2-D Ray tracing (Metrics)
- Geopotential Function
- Hydrostatic Model
- Geometric and Attitude Model
- Scan Model
- Refraction

The forms of many of the equations in this work have direct analogs in the scalar ATBD, and much of the critical details involving integration and removal of singularities will not be repeated here.

3.1 EOS MLS Viewing Geometry

The Instrument Field Of View Polarized Pointing(IFOVPP) coordinate system is defined such that the instrument boresight is in the $-\hat{z}$ direction and receives polarized radiation with its Poynting vector in the $\hat{z}$ direction, whose electric field is in the $\hat{x}$ direction, and whose magnetic field is in the $\hat{y}$ direction. The geomagnetic field, $\boldsymbol{\mathcal{H}}_{\text{geo}}$, is oriented at an angle θ to the $\hat{z}$ direction. The geomagnetic field vector and $\hat{z}$-axis form a plane that is rotated through ϕ relative to the x-z plane. In this linear polarization basis, components with $\vec{\boldsymbol{E}}$ in the $\hat{x}$ direction are designated "co-polarized" and those with $\vec{\boldsymbol{E}}$ in the $\hat{y}$ direction are designated

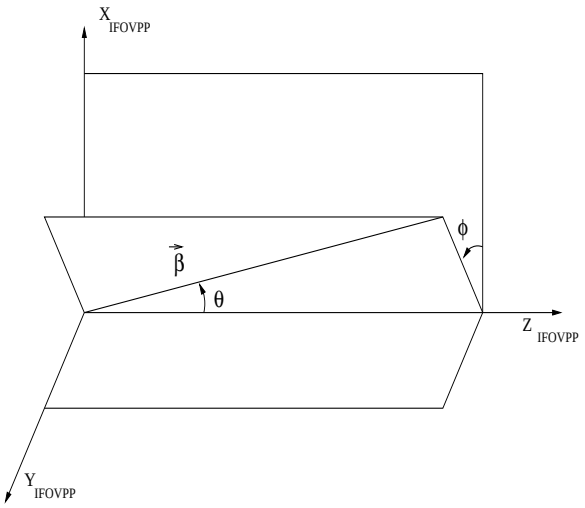

Figure 3.1: Angle definition for polarized radiative transfer. In the Instrument Field Of View Polarized Pointing (IFOVPP) coordinate system, $\hat{x}$ is the antenna $\hat{E}$ direction, $\hat{y}$ is the antenna $\hat{H}$ direction, $\hat{z}$ is the radiation propagation direction.

"cross-polarized". The state vector contains the atmospheric state on layer boundaries. The layer indexing scheme is shown in Figure 2.1.

3.2 Incremental Opacity Integral

As was shown in Chapter 2, polarized radiative transfer depends upon a tensor transmittance, $\boldsymbol{\mathcal{T}}$, which is constructed from exponentials of slab incremental optical opacities, which in turn are the integrals of the propagation matrix, $\boldsymbol{G}$.

$$\boldsymbol{I}(x) = \sum_{i=1}^{2N+1} \boldsymbol{\mathcal{T}}_i \, \Delta B_i \; , \tag{3.1}$$

where

$$\begin{aligned}
\boldsymbol{\mathcal{T}}_i &= \boldsymbol{P}_i \, \boldsymbol{P}_i^{\dagger} \; , \\
\boldsymbol{P}_i &= \boldsymbol{P}_{i-1} \, \boldsymbol{E}_i \; , \\
\boldsymbol{E}_i &= \exp - \int_{s_i}^{s_{i-1}} \boldsymbol{G}(s') \, ds' \; , \\
\boldsymbol{E}_1 &= \boldsymbol{P}_1 = \boldsymbol{1} \; .
\end{aligned}$$

The form of the polarized incremental opacity is very similar to that in the scalar model, and here we will adopt the scalar model's notation:

$$\sum_{k}^{\text{species}} \boldsymbol{\Delta\delta}_{i \to i-1}^{k} \equiv \int_{s_i}^{s_{i-1}} \boldsymbol{G}(s') ds' .$$

This notation has the advantage that it explicitly states the boundaries between which integration is to be performed. In the production code, the indexing across the tangent point gets hairy, and bugs can be hard to find. Also, in the sum over k, it explicitly allow the contributions of other species, with the field opacity of unpolarized species (half of their power opacities) added to $\boldsymbol{G}$ as multiple of the identity.

The expression given below includes a correction for refraction. Refraction only becomes significant for tangent heights below 20 km, and the oxygen line in Band 22 and Band 26 is opaque high in the atmosphere. However, inclusion of the refraction correction allows the polarized model to be used more generally, and can give a consistent expression, both for the line centers and wings.

The incremental opacity integral due to polarized O_2 lines is

$$\boldsymbol{\Delta\delta}^{\mathrm{O_2}}_{i\to i-1} = \frac{\Delta s^{\mathrm{refr}}_{i\to i-1}}{\Delta s_{i\to i-1}} \sum_{\Delta M=-1}^{+1} \boldsymbol{\rho}_{_{\Delta M}}(\theta,\phi)\, \xi_{_{M,\Delta M}} \int_{\zeta_i}^{\zeta_{i-1}} \mathsf{f}^{\mathrm{O_2}}(\zeta,\phi(\zeta))\, \beta_{\Delta M}\left(\zeta, \mathcal{B}(\zeta), T\left(\zeta\right), \nu\right) \frac{\mathrm{d}s}{\mathrm{d}h} \frac{\mathrm{d}h}{\mathrm{d}\zeta}\, \mathrm{d}\zeta, \tag{3.2}$$

where $\xi_{_{M,\Delta M}}$ is from Table 1.2, $\mathsf{f}^{\mathrm{O_2}}(\zeta,\phi(\zeta))$ is the O_2 species representation basis. Here, we are chain-ruling from pathlength s to height h to negative-log-pressure, ζ.

$$\begin{aligned}
\frac{\mathrm{d}s}{\mathrm{d}h} &= \frac{\left(h\left(\zeta\right) + R^{\oplus}_{\mathrm{eq}}\left(\phi\left(\zeta\right)\right)\right)}{\sqrt{\left(h\left(\zeta\right) + R^{\oplus}_{\mathrm{eq}}\left(\phi\left(\zeta\right)\right)\right)^2 - \left(h\left(\zeta_t\right) + R^{\oplus}_{\mathrm{eq}}\left(\phi\left(\zeta_t\right)\right)\right)^2}} \\
&\text{and} \\
\frac{\mathrm{d}h}{\mathrm{d}\zeta} &= \frac{\left[h\left(\zeta\right) + \overset{\star}{R}_o\left(\phi\left(\zeta\right)\right) - R_o\left(\phi\left(\zeta\right)\right) + R^{\oplus}\left(\phi\left(\zeta\right)\right)\right]^2 T\left(\zeta\right) k \ln 10}{g_o\left(\phi\left(\zeta\right)\right) \overset{\star}{R}{}^2_o\left(\phi\left(\zeta\right)\right) \mathcal{M}\left(\zeta\right)}.
\end{aligned} \tag{3.3}$$

These expressions are discussed more fully in the scalar forward model ATBD. [10]

As is discussed in Section 1.3, the $\boldsymbol{\rho}$ terms are purely functions of the orientation of the propagation direction with respect to the geomagnetic field. They contain all of the angular dependence and all of the 2x2 tensor-nature of the expression. These terms are common for all lines with the same ΔM, though in the case of the 118-GHz line, there is only one Zeeman component for each ΔM. All of the other terms in this expression are (possibly complex) scalars. In the IFOVPP frame,

$$\begin{aligned}
\boldsymbol{\rho}_{\pm 1} &= \begin{bmatrix} \cos^2\phi + \sin^2\phi\cos^2\theta & -\sin\phi\cos\phi\sin^2\theta \mp \imath\cos\theta \\ -\sin\phi\cos\phi\sin^2\theta \pm \imath\cos\theta & \sin^2\phi + \cos^2\phi\cos^2\theta \end{bmatrix}, \\
\boldsymbol{\rho}_{0} &= \begin{bmatrix} \sin^2\phi\sin^2\theta & \sin\phi\cos\phi\sin^2\theta \\ \sin\phi\cos\phi\sin^2\theta & \cos^2\phi\sin^2\theta \end{bmatrix}.
\end{aligned} \tag{3.4}$$

or, more transparently,

$$\boldsymbol{\rho}_{\pm 1} = \boldsymbol{R}_\phi \begin{bmatrix} 1 & \mp\imath\cos\theta \\ \pm\imath\cos\theta & cos^2\theta \end{bmatrix} \boldsymbol{R}^{\dagger}_{\phi} \tag{3.5}$$

$$\boldsymbol{\rho}_{0} = \boldsymbol{R}_\phi \begin{bmatrix} 0 & 0 \\ 0 & \sin^2\theta \end{bmatrix} \boldsymbol{R}^{\dagger}_{\phi} \tag{3.6}$$

where

$$\boldsymbol{R}_\phi = \begin{bmatrix} \cos\phi & \sin\phi \\ -\sin\phi & \cos\phi \end{bmatrix}. \tag{3.7}$$

3.2.1 Unpolarized Contributions to Incremental Opacity

The contributions of unpolarized species may be included by adding half of their scalar power incremental opacities, $\Delta\delta^k_{i\rightarrow i-1}$, to the diagonal of the the tensor field incremental opacity. The one half changes *power* incremental opacity to *field* incremental opacity. Equivalently, the scalar incremental opacities may be added with weights $(\frac{1}{4}, \frac{1}{2}, \frac{1}{4})$ to the total of everything that multiplies $\boldsymbol{\rho}_-$, $\boldsymbol{\rho}_0$ and $\boldsymbol{\rho}_+$, respectively.

3.2.2 Cross-Section $\boldsymbol{\beta}$

Field cross-sections for the polarized lines are identical to the *power* cross-sections in the scalar model except they are reduced by a factor of two and they require complex lineshapes rather than only the real parts. Polarized power transmittance, $\boldsymbol{\mathcal{T}}$, is formed from products of pairs of field transmittances, which are exponentials of the cross-sections. The two half power cross-sections will add so that each of the diagonal elements will correctly give the scalar result for unpolarized radiation.

The field cross-section β^k for the kth species is

$$\beta^k = \frac{1}{2}\,\mathcal{R}^k\,\sqrt{\frac{\ln 2}{\pi}}\frac{10^{-13}}{kTw_d^k}\,P\sum_j 10^{\mathcal{S}_j^k}F\left(x_j^k, y_j^k, z_j^k\right) \tag{3.8}$$

where

$$\begin{aligned}\mathcal{S}_j &= \mathcal{I}_j\left(T_0\right) + \log\left[\frac{Q^k(T_0)}{Q^k(T)}\right] + \frac{hc}{k}E''^k_j\left(\frac{1}{T_0}-\frac{1}{T}\right)\\ &+ \log\left[\tanh\left(\frac{h\nu}{2kT}\right)\right] + \log\left[\frac{1+\exp\left\{-h\nu_j/kT\right\}}{1-\exp\left\{-h\nu_{0j}/kT_0\right\}}\right].\end{aligned}$$

- $\mathcal{R}^k$ is the isotopic fraction,
- T is temperature in Kelvins,
- T_0=300K,
- P is pressure in hPa,
- $\mathcal{I}_j\left(T_0\right)$ is the logarithm of the integrated intensity in nm^2MHz at T_0,
- ν_{pj} is the pressure-shifted (but not Doppler-shifted) line center frequency in MHz,
- ν_{0j} is the unshifted line frequency, as it appears in the JPL Catalog.
- E''^k_j is the lower-state energy for the jth transition in cm^{-1},
- $Q^k(T_0)$ is the partition function at T_0,
- $Q^k(T)$ a log-linear interpolation of tabulated partition function values,
- $w_d = 3.58117369\times10^{-7}\nu\sqrt{\frac{T}{\mathcal{M}}}$ is the Doppler width,
- $\mathcal{M}$ is the absorber molecular mass,

- F_j is the complex lineshape function,
- the subscript j identifies the individual lines in the molecule.

3.2.3 Lineshape

The lineshape that we use for each of the Zeeman components is the Fadeeva, or complex error function, modified to include line interference. Fadeeva includes the convolution of a Gaussian thermal Doppler lineshape with a Lorentzian collisional lineshape. It has a simple form,

$$\mathcal{F}(z) = \frac{i}{\pi} \int_{-\infty}^{\infty} \frac{e^{-t^2}}{z - t}\, dt$$

for complex z, or

$$\begin{aligned} \mathcal{F}(x + iy) =& \frac{1}{\pi} \int_{-\infty}^{\infty} e^{-t^2} \left(\frac{y}{(x-t)^2 + y^2} + \frac{i(x-t)}{(x-t)^2 + y^2} \right) dt \\ =& \mathcal{U}(x, y) + i\mathcal{V}(x, y) \end{aligned} \tag{3.9}$$

The real part of Fadeeva, $\mathcal{U}(x, y)$, is the Voigt function, which is the lineshape used in the scalar forward model. Terms involving line mixing coefficients, Y, are added to include the first-order effects of interference with the lines of the 60-GHz band [11]. The tabulated, zero-field mixing coefficient will be used for all three Zeeman components. The contribution of these terms is negligible for the pressures where Zeeman-splitting is resolved, but they are included so that this model will merge more smoothly with the scalar model. Line interference can only occur between Zeeman components of the same Δm, so there is no interference among the Zeeman components of the 118-GHz oxygen line.

The modified Fadeeva lineshape which we will use is

$$\begin{aligned} F(x_j, y_j) &= \frac{1}{\pi} \frac{\nu}{\nu_{0j}} \int_{-\infty}^{\infty} e^{-t^2} \left(\frac{y_j - Y_j(x_j - t)}{(x_j - t)^2 + y_j^2} + \frac{i(y_j Y_j + x_j - t)}{(x_j - t)^2 + y_j^2} \right) dt \\ &= \frac{\nu}{\nu_{0j}} (1 + iY_j) \mathcal{F}(x_j + iy_j), \end{aligned} \tag{3.10}$$

where

$$\begin{aligned} x_j &= \frac{\sqrt{\ln 2}\,(\nu - \nu_j - \Delta\nu_{j,m,\Delta m})}{w_d^k}, \\ y_j &= \frac{\sqrt{\ln 2}\, w_{cj} P}{w_d^k} \left(\frac{T_0}{T} \right)^{n_{cj}^k}, \\ Y_j &= P \left[\delta_j^k \left(\frac{T_0}{T} \right)^{n_{\delta_j}^k} + \gamma_j^k \left(\frac{T_0}{T} \right)^{n_{\gamma_j}^k} \right], \\ w_d^k &= \sqrt{2 \ln 2\, \mathrm{k_B}/c} \sqrt{\frac{T}{\mathcal{M}^k}}\, \nu, \end{aligned}$$

and the line center frequency is shifted according to

$$\nu_j^k = \left[\nu_{0j}^k + \Delta\nu_{0j}^k P \left(\frac{T_0}{T} \right)^{n_{\Delta\nu_{0j}}^k} \right] \left(1 + \frac{v_{\mathrm{los}}}{c} \right). \tag{3.11}$$

Line constants from the JPL Catalog [9], which are tabulated in the scalar forward model ATBD [10], include unshifted line center frequency, ν_{0j}, collisional linewidth parameter, w_{cj}^k, collisional linewidth temperature dependence exponent, n_{cj}^k, line pressure shift parameter, $\Delta\nu_{0j}^k$ line pressure shift temperature dependence exponent, $n_{\Delta\nu_{0j}}^k$ and line interference parameters, δ_j^k, $n_{\delta_j}^k$, γ_j^k, $n_{\gamma_j}^k$.

The Doppler width depends upon $\mathcal{M}^k$, the molecular mass of species k, and upon v_{los}, the line-of-sight velocity (which is positive if the observer and atmosphere are moving toward one another.) The Zeeman frequency shifts $\Delta\nu_{j,M,\Delta M}$ from Table 1.2. are included in $x_{j,M,\Delta M}$. The leading $\frac{\nu}{\nu_{0j}}$, which gives agreement with the Debye non-resonant shape at low frequencies, is nearly constant over the Doppler width and is pulled outside of the integral..

The cross section is summed over all of the lines that contribute significantly. The z_j dependence of "Lineshape(x_j, y_j, z_j)" in the scalar ATBD explicitly includes the negative-frequency resonance of each line. These terms give the absorption due to the far wing of the emission line at $-\nu_{0j}$.

The polarized model's lineshape, $F(x_j, y_j)$, does not include these negative frequency terms. If the tail of the line at -118 GHz is considered significant, it can be included in the list of lines to be modeled, but as we are not including many strong lines in the 60-GHz band, 60 GHz away from our band of interest, there is no need to single out the -118-GHz line, four times more distant, for special treatment.

Accurate and efficient evaluation of the Fadeeva lineshape and its derivatives has been an area of continuing research in the MLS group, with significant contributions made by Zvi Shippony [14].

3.3 Geomagnetic Field Model

3.3.1 IGRF

The International Geomagnetic Reference Field (IGRF) model [2][3] is the empirical representation of the Earth's magnetic field recommended for scientific use by the International Association of Geomagnetism and Aeronomy (IAGA). The IGRF model represents the main (core) field, $\boldsymbol{\mathcal{B}}_{\text{geo}}$, without external sources. The model employs the usual spherical harmonics expansion of the scalar potential in geocentric coordinates. The IGRF model coefficients are based on all available data sources including geomagnetic measurements from observatories, ships, aircraft and satellites.

The launch-ready version of the EOS-MLS polarized forward model (version 1.4 of the level 2 software) uses IGRF, without any additional external sources. In the absence of magnetic storms and outside of the auroral belts, we expect that field variation at the altitudes below 120 km will be on the order of 5 percent, but there is significant uncertainty in this value. The adequacy of the IGRF model will be a research topic.

Since the magnetic susceptibility of the atmosphere is very nearly unity (in Gaussian units) we use $\boldsymbol{\mathcal{B}}_{\text{geo}}$for $\boldsymbol{\mathcal{H}}_{\text{geo}}$in the Zeeman expressions.

The ECR components of magnetic field are loaded into profiles of the state vector by the level 2 code and are treated like any other geophysical parameter. The machinery of the forward model interpolates these ECR values to positions along the integration path. The ECR values are then rotated to the IFOVPP frame for each pointing.

3.3.2 Rotation of Field to IFOVPP

The IGRF model provides the Earth's core magnetic field in Earth-Center-Rotating (ECR) coordinates, since the field is fixed in the solid earth. For the purpose of polarized forward modeling, we want the geomagnetic field in coordinates of the instrument field of view and polarization.

Fortunately, the hard work has been done for us by the EOSDIS Science Data Production (SDP) Toolkit [1], which provides minor-frame-dependent ECR-to-ECI and ECI-to-Spacecraft rotations, and in the "EOS MLS Calibration Report" [5], which includes the information needed to rotate from spacecraft coordinates to the field of view of each of the radiometers. The FOV defined in the Calibration Report, Volume 2, p.704, has its $+\hat{z}$ along the antenna boresight and $\hat{x}$ in the direction of the magnetic field vector, so this frame of reference may be transformed to IFOVPP by $\hat{z} \rightarrow -\hat{z}$, $\hat{x} \rightarrow \hat{y}$, $\hat{y} \rightarrow \hat{x}$. Rotation matrices from ECR to IFOVPP for R1A are calculated during level-1 processing and are included as part of the L1BOA files. In the initial version of the software there is no separate rotation matrix for R1B, but the cross-polarization of the R1A pointing may be used as proxy. I should investigate the magnitude of the error introduced here.

The ECR-to-IFOVPP matrices are provided to the forward model as "MIF" quantities, for the polarization and pointing of the central axis of the R1A antenna at the middle of each integration (MIF). The forward model does radiative transfer calculations, for a grid of pointings, which will later be convolved with each MIF's antenna pattern. We need ECR-to-IFOVPP on the forward model pointing grid, not as a MIF quantity. Rather than interpolate (and extrapolate) the rotation matrices from the MIF grid to the radiative transfer pointing grid, we use the rotation matrix from the closest MIF. Points in the radiative transfer grid that are above the center of the highest MIF all use the rotation matrix from the highest MIF, but errors induced should be negligible compared to those from other sources of uncertainty in the magnetic field.

3.4 Derivatives

3.4.1 General Form of Polarized Derivatives

Equation 3.1 may be differentiated with respect to a state vector element, x, to give a derivative as required by the retrieval. As always, care must be taken in the tensor case to preserve matrix order.

$$\begin{aligned} \frac{\partial \boldsymbol{I}(x)}{\partial x} &= \frac{\partial}{\partial x} \sum_{i=1}^{2N} \boldsymbol{\mathcal{T}}_i \, \Delta B_i \\ &= \sum_{i=1}^{2N} \frac{\partial \boldsymbol{\mathcal{T}}_i}{\partial x} \, \Delta B_i + \boldsymbol{\mathcal{T}}_i \, \frac{\partial \Delta B_i}{\partial x} \end{aligned} \tag{3.12}$$

and we recall Equation 2.37,

$$\boldsymbol{\mathcal{T}}_i \equiv \boldsymbol{P}_i \, \boldsymbol{P}_i^{\dagger} \, .$$

The derivative of $\boldsymbol{\mathcal{T}}_i$ may be built up, for successive layers, by differentiating the recurrence relation $\boldsymbol{P}_i = \boldsymbol{P}_{i-1}\boldsymbol{E}_{i-1}$.

$$\frac{\partial \boldsymbol{P}_i}{\partial x} = \frac{\partial \boldsymbol{P}_{i-1}}{\partial x}\boldsymbol{E}_{i-1} + \boldsymbol{P}_{i-1}\frac{\partial \boldsymbol{E}_{i-1}}{\partial x} \tag{3.13}$$

with

$$\frac{\partial \boldsymbol{\mathcal{T}}_i}{\partial x} = \frac{\partial \boldsymbol{P}_i}{\partial x}\boldsymbol{P}_i^\dagger + \left(\frac{\partial \boldsymbol{P}_i}{\partial x}\boldsymbol{P}_i^\dagger\right)^\dagger. \tag{3.14}$$

(Thanks to Fred Krogh for suggesting this approach.)

3.4.2 Mixing Ratio Derivatives

The expression for incremental opacity is a sum of the product of the mixing ratios and their derivatives, so the derivatives themselves are easily calculated by dropping f^k and the summation over species k from Equation 3.2.

$$\frac{\partial \boldsymbol{\Delta\delta}^k_{i\to i-1}}{\partial f^k_{lmn}} = \sum_{\Delta M=-1}^{+1} \boldsymbol{\rho}_{\Delta M}(\theta,\phi)\int_{\zeta_i}^{\zeta_{i-1}} \beta^k_{\Delta M}(\zeta,\nu,T,\mathcal{B})\frac{\mathrm{d}s}{\mathrm{d}h}\frac{\mathrm{d}h}{\mathrm{d}\zeta}\,\mathrm{d}\zeta \tag{3.15}$$

Mixing ratio coefficients are f^k_{lmn} where k refers to the species, l is vertical coordinate (ζ), m is horizontal coordinate (ϕ) and n is frequency (ν). Frequency is included for the case of "extinction," which may be treated as a frequency dependent species.

The incremental polarized transmission derivative, $\frac{\partial \boldsymbol{E}}{\partial f}$, is evaluated using Equation A.3 with Equation 3.15 as its argument. the result is substituted into Equation 3.13 to get $\frac{\partial \boldsymbol{P}}{\partial f}$, which is, in turn, substituted into Equation 3.14 to get $\frac{\partial \boldsymbol{\mathcal{T}}}{\partial x}$. Substituting this result into Equation 3.12 gives $\frac{\partial \boldsymbol{I}}{\partial x}$.

The term in Equation 3.12 involving $\frac{\partial \Delta B_k}{\partial x}$ is zero because ΔB_k depends only upon temperature.

Generally, we do not attempt to retrieve a $^{16}O_2$ mixing ratio, and consider oxygen to comprise a constant fraction of dry air. The dilution of dry air by water vapor is only appreciable in the lower troposphere; EOS-MLS bands 22 and 26, for which this polarized model is being developed, will never see to this depth. The $^{16}O_2$ mixing ratio starts to fall off in the thermosphere ($>$ 80km) as an appreciable fraction of the molecules begin to dissociate. However, at these pressures, the lines are Doppler broadened and there is not enough information to separate temperature from mixing ratio even if a retrieval were attempted. The initial plan for EOS-MLS retrievals is to use, as truth, the same *a priori* $^{16}O_2$ mixing ratio profile that was used for UARS.

3.4.3 Temperature Derivatives

Much of what is said in the section of the scalar ATBD devoted to temperature derivatives is applicable here. Temperature differentiation is quite complicated because the atmospheric absorption, the source function and the path length (through the hydrostatic model) all depend upon temperature. The equations follow the same forms as in scalar ATBD, but with a β for each ΔM multiplying an appropriate tensor, $\boldsymbol{\rho}$, and summation over ΔM.

Temperature coefficients, with respect to which we want to differentiate, are f_{lm}^T where l is vertical coordinate (ζ) and m is horizontal coordinate (ϕ).

As in the scalar case, a simplified incremental opacity is used that neglects the temperature dependence in refraction and uses a simplified $\frac{dh}{d\zeta}$. The frequency representation basis is dropped since temperature has no frequency dependence. The simplified incremental opacity has the form

$$\Delta\delta_{i\to i-1}^k = \frac{\Delta s_{i\to i-1}^{\text{refr}}}{\Delta s_{i\to i-1}} \sum_{\Delta M=-1}^{+1} \boldsymbol{\rho}_{\Delta M}(\theta,\phi) \int_{\zeta_i}^{\zeta_{i-1}} \mathsf{f}^k\left(\zeta,\phi\left(\zeta\right),\nu\right) \beta_{j,\Delta M}^k\left(\zeta,\nu,T,\mathcal{B}\right) \times \frac{H^3}{\sqrt{H^2-H_t^2}} \frac{Tk\ln 10}{g_o R_o^2 \mathcal{M}} \,\mathrm{d}\zeta \tag{3.16}$$

$$\begin{aligned}\frac{\mathrm{d}\Delta\delta_{i\to i-1}^k}{\mathrm{d}f_{lm}^T} = \frac{\Delta s_{i\to i-1}^{\text{refr}}}{\Delta s_{i\to i-1}} \sum_{\Delta M=-1}^{+1} \boldsymbol{\rho}_{\Delta M}(\theta,\phi) \\ \times \int_{\zeta_i}^{\zeta_{i-1}} \Bigg\{ \mathsf{f}^k \frac{\partial\beta_{j,\Delta M}^k(\zeta)}{\partial \mathsf{f}_{lm}^T} \eta_l^T\left(\zeta\right)\eta_m^T\left(\phi\left(\zeta\right)\right) \frac{\mathrm{d}s}{\mathrm{d}h}\frac{\mathrm{d}h}{\mathrm{d}\zeta} \\ + \mathsf{f}^k\beta_{j,\Delta M}^k(\zeta) \frac{2H^2\frac{\mathrm{d}H}{\mathrm{d}f_{lm}^T} - 3H_t^2\frac{\mathrm{d}H}{\mathrm{d}f_{lm}^T} + HH_t\frac{\mathrm{d}H_t}{\mathrm{d}f_{lm}^T}}{\left(H^2-H_t^2\right)^{\frac{3}{2}}} \frac{\mathrm{d}h}{\mathrm{d}\zeta} \\ + \mathsf{f}^k\beta_{j,\Delta M}^k(\zeta) \frac{\eta_l^T\left(\zeta\right)\eta_m^T\left(\phi\left(\zeta\right)\right)}{T} \frac{\mathrm{d}s}{\mathrm{d}h}\frac{\mathrm{d}h}{\mathrm{d}\zeta} \Bigg\} \mathrm{d}\zeta\end{aligned} \tag{3.17}$$

Apart from the summation over ΔM and the $\boldsymbol{\rho}$ matrices, this expression is identical to what is in the scalar forward model except that here we have both the real and imaginary parts of the lineshape to deal with in the temperature derivative of β. The part of the this derivative which differs from the expression in the scalar ATBD is the derivative of the lineshape. We have, from Equation 3.10,

$$F(x_j,y_j) = \frac{\nu}{\nu_{0j}}(1+iY_j)[\mathcal{U}(x_j,y_j)+i\mathcal{V}(x_j,y_j)]$$

so

$$\begin{aligned}\frac{\mathrm{d}F(x_j,y_j)}{\mathrm{d}T} = \frac{\nu}{\nu_{0j}}\Bigg[(1+iY_j)\frac{\mathrm{d}\mathcal{U}}{\mathrm{d}x}\frac{\mathrm{d}x}{\mathrm{d}T} + (1+iY_j)\frac{\mathrm{d}\mathcal{U}}{\mathrm{d}y}\frac{\mathrm{d}y}{\mathrm{d}T} + i\frac{\mathrm{d}Y}{\mathrm{d}T}\mathcal{U} \\ + i(1+iY_j)\frac{\mathrm{d}\mathcal{V}}{\mathrm{d}x}\frac{\mathrm{d}x}{\mathrm{d}T} + i(1+iY_j)\frac{\mathrm{d}\mathcal{V}}{\mathrm{d}y}\frac{\mathrm{d}y}{\mathrm{d}T} - \frac{\mathrm{d}Y}{\mathrm{d}T}\mathcal{V}\Bigg]\end{aligned} \tag{3.18}$$

From this point, substitutions may be made from the scalar ATBD. The derivatives of the real and imaginary parts of Fadeeva are

$$\begin{aligned}\frac{\partial\mathcal{U}}{\partial y} = \frac{\partial\mathcal{V}}{\partial x} = 2y\mathcal{V} - 2x\mathcal{U}, \\ \frac{\partial\mathcal{U}}{\partial x} = -\frac{\partial\mathcal{V}}{\partial y} = 2y\mathcal{V} + 2x\mathcal{U} - 2/\sqrt{\pi},\end{aligned} \tag{3.19}$$

and from Equation 9.8 of the scalar ATBD,

$$\begin{aligned}
\frac{\mathrm{d}\nu_j^k}{\mathrm{d}T} &= \frac{(\nu_{0j}^k v_c - \nu_j^k) n_{\Delta\nu_{0j}}^k}{T} \\
\frac{\mathrm{d}x_j^k}{\mathrm{d}T} &= -\frac{x_j^k}{2T} - \frac{\sqrt{\ln 2}\,(\nu_{0j}^k v_c - \nu_j^k) n_{\Delta\nu_{0j}}^k}{T w_d^k} \\
\frac{\mathrm{d}y_j^k}{\mathrm{d}T} &= -\frac{y_j^k (n_{cj}^k + \frac{1}{2})}{T} \\
\frac{\mathrm{d}Y_j^k}{\mathrm{d}T} &= -P \left[\frac{n_{\delta_j}^k \delta_j^k}{T} \left(\frac{T_0}{T} \right)^{n_{\delta_j}^k} + \frac{n_{\gamma_j}^k \gamma_j^k}{T} \left(\frac{T_0}{T} \right)^{n_{\gamma_j}^k} \right]
\end{aligned} \tag{3.20}$$

This expression for the temperature derivative of β replaces the power-law approximation which was used in the UARS code. This expression involves the analytic derivative of the lineshape and is somewhat daunting, but results in a 30 percent speed-up of the temperature-derivative code. The power-law dependence gave derivatives in good agreement with the analytic case, but required evaluations of β at two perturbed temperatures.

3.4.4 $\boldsymbol{\beta}$ Derivatives

Derivatives of quantities on which $\Delta\delta_{i+1\to i}^k$ has dependence only through β can be written

$$\frac{\partial \boldsymbol{\Delta\delta}_{i\to i-1}^k}{\partial x_j} = \sum_{\Delta M=-1}^{+1} \boldsymbol{\rho}_{\Delta M}(\theta,\phi) \int_{\zeta_i}^{\zeta_{i-1}} f_{lmn}^k \, \frac{\mathrm{d}\beta_{\Delta M}^k}{\mathrm{d}x_j} \, \frac{\mathrm{d}s}{\mathrm{d}h} \, \frac{\mathrm{d}h}{\mathrm{d}\zeta} \, \mathrm{d}\zeta \; . \tag{3.21}$$

This class includes derivatives with respect to spectroscopic parameters, wind-induced Doppler shifts, and magnetic field.

Derivatives with respect to line center frequency ν_j will be used in the retrieval of Doppler shifts that result from large-scale wind along the line-of-sight. Doppler shifts due to the spacecraft velocity are already accounted for in the line center frequencies. We expect to encounter winds at 90 km on the order of 70 m/s in the N-S (meridional) direction (mostly along the line of sight) and 100 m/s in the E-W (zonal) direction; a 70 m/s wind will result in a 3-KHz line shift. This is a small fraction of the DACS channel spacing, but simulations indicate that it should be measurable with sufficient averaging.

Derivatives with respect to the linewidth may be useful for retrieval of a width that may be dominated by unmodeled variation in the magnetic field strength along the integration path. Such variation will move the σ lines in and out, causing them to be blurred, and making the σ lines appear broader than the π line

These are all areas for research after launch.

3.5 Field of View Convolution

Convolution of polarized radiances with the instrument antenna patterns is nearly identical to what is described in the scalar Forward Model ATBD [10] in the chapter *Field of View Integration*. In both cases, one starts with an expression for the polarized, far-field antenna pattern, $\boldsymbol{\mathcal{G}}$, which is a function of offset in elevation and azimuth (ϵ, α) from the tangent

pointing elevation and azimuth (ϵ_t, α_t) which label the MIF to be modeled. Ideally, $\boldsymbol{\mathcal{G}}$ would be convolved with radiances $\boldsymbol{I}$, which in the scalar case are radiance times the identity matrix.

$$I(\epsilon_t, \alpha_t) = \frac{1}{4\pi}\mathrm{Tr}\int_0^{2\pi}\int_{-\frac{\pi}{2}}^{\frac{\pi}{2}} \boldsymbol{I}(\epsilon, \alpha)\,\boldsymbol{\mathcal{G}}(\epsilon_t, \alpha_t; \epsilon, \psi)\cos\epsilon\,\mathrm{d}\epsilon\,\mathrm{d}\alpha \tag{3.22}$$

This expression sums the convolutions over each of the four degrees of freedom in the radiances: co-polarized, cross-polarized, circular-coherence and linear-coherence. Near-field measurements of the MLS antenna patterns [5] show the total power in the cross-polarized patterns of the R1A and R1B receivers to be down 25 to 30 dB from the co-polarized total power. Linear and circular coherences probably vary over the pattern, but have not been measured.

In the scalar case, the radiation field is assumed to be unpolarized and the tensor equation reduces to a scalar convolution of the scalar radiance with the sum of the co-polarized and cross-polarized antenna patterns.

In the polarized case, we have chosen to do our radiative transfer in the IFOVPP basis, so that the antenna pattern is very nearly zero in all but its (1,1) component. The polarized case is handled by taking the co-polarized component of the radiance and then treating it exactly like an unpolarized radiance from the scalar code.

$$I_{\parallel} \rightarrow I_{\mathrm{unpolarized}}$$

Ideally, the cross-polarization and the co-polarization would each be convolved with its own pattern and then added. The approximation made here is the replacement of cross-polarized radiances with co-polarized radiances. Resulting errors are on the order of the difference in the unconvolved radiances reduced by 25–30 dB. In the most sensitive case, where there could be as much as a 200 K contrast between the two modes, neglect of the cross-polarized term might result in a 0.5 K error in a modeled radiance, but this would only be in the highest tangent pointings where other sources of error will dominate. Inclusion of a small, fixed fraction of $I_{\perp}$ in the scalar I carried away from the polarized radiative transfer module could be accomplished easily, and may be the topic of further research.

From this point, the scalar frequency averaging model is followed exactly, with the Band 22 and Band 26 polarized dacs channels treated exactly as are the scalar Bands 23, 24, and 25. DACS spectral convolution is described in Chapter 4.

Chapter 4

DACS Spectral Integration

4.1 DACS Spectral Integration

Each digital autocorrelator spectrometer (DACS) has 129 channels equally spaced across a 12.5-MHz band in the center of a 25-channel filterbank. The signal into a DACS is supplied by a single-sideband mixer with its local oscillator (LO) at 905-MHz in the second IF. The upper sideband rejection is approximately -27 dB and an anti-aliasing filter limits the lower sideband to approximately 10 MHz from 905-895 MHz. The input signal to a DACS is sampled at 25 MHz and fed into a 129-lag autocorrelator. The Fourier transform of the accumulated autocorrelation is 129 channels with centers spaced 12.5/128 MHz from 905 MHz down to 892.5 MHz.

To first order, each channel's passband has a sinc(x)=sin(x)/x character, where $x = \pi\,(\nu - \nu_{\rm ch})\,128/12.5$ MHz and $\nu_{\rm ch}$ is the channel's center frequency. This filter shape results from the sharp cutoff of the autocorrelation after the 128th lag in the time domain. The sinc(x) of each channel is centered at the channel center and has a zero at the center of each of the other channels. These sinc filter shapes must be modified to reflect the variations in gain across the passband due to the anti-aliasing filter and amplifier characteristics. Even for an ideal DACS, filter shapes for the channels would differ from one another, as shown in Figure 4.1, because of the contributions of image channels.

The forward model must be calculated on an oversampled grid (higher than the channel spacing) for the filter shapes to have any impact. Oversampling by a factor of two gives a point on each of the sinc peaks as well as a wasted point on each of the zeros. Oversampling the channel spacing by a factor of four gives three points between each zero. The amount of oversampling required depends upon the sharpness of the spectral features to be modeled.

DACS channel responses may be modeled by brute force, multiplying a fine grid of discrete-frequency forward model results by a grid of frequency weights for each of the 129 channels, but this calculation is more efficiently done in the Fourier domain.

We want to convolve an array of calibrated monochromatic radiances, $R(\nu_i)$, with normalized DACS channel responses to produce calibrated DACS channel responses, T_k. In addition to $R(\nu_i)$, we require a normalized "pre-filter shape," $P(\nu_i)$, which is the product of all of the gain variation across amplifiers and comparators in the signal chain as well as the DACS anti-aliasing filter and $L(\nu_i)$, which is the convolved spectral shape of the first local oscillator (LO) in the mixer chain. We want $R(\nu_i)$, $P(\nu_i)$ and $L(\nu_i)$ to be sampled on a grid of frequencies ν_i that is finer than the channel spacing by a factor of 2x or 4x so that we can

Figure 4.1: This example shows the 6th channel of a hypothetical 20-channel DACS. The upper panel shows the sinc filter shape while the lower shows the actual response, which is the sum of the sinc and all of its images. The EOS-MLS DACS have 129 channels so the filter shapes of middle channels are much more sinc-like than what is shown here.

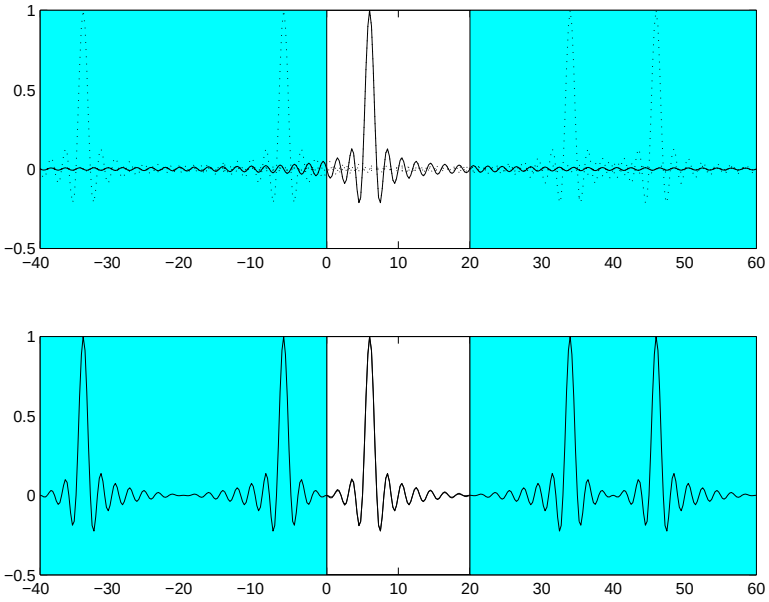

see the impact of the sinc's bumps between the channel centers. In practice, P and L are measured using the DACS themselves, so they are measured at precisely the DACS channel spacing. Fortunately, reasonable extrapolations of these functions can be performed in the time domain.

We will assume that we begin with $R(\nu_i)$, $P(\nu_i)$ and $L(\nu_i)$ on a grid that is 4x finer than the DACS channel spacing. These functions' time-domain pairs are denoted by lowercase letters.

$$\begin{aligned} R(\nu_i) &\stackrel{DCT}{\longrightarrow} r(t_j)\ , \\ P(\nu_i) &\stackrel{DCT}{\longrightarrow} p(t_j)\ , \\ L(\nu_i) &\stackrel{DCT}{\longrightarrow} l(t_j)\ , \end{aligned} \tag{4.1}$$

where DCT is the "Discrete Cosine Transform."

First we convolve the input signal with the LO shape and multiply the result by the pre-filter shape:

$$A = (R \star L)P = \mathrm{DCT}^{-1}(rl)P\ , \tag{4.2}$$

where $\star$ is convolution. This is all at high (4x) resolution. Then we forward, 513-element DCT, truncate from 513 to 129 lags (time samples), and then perform a 129-element inverse DCT.

$$A' = \mathrm{DCT}_{129}^{-1}(\mathrm{DCT}_{513}(A))) \tag{4.3}$$

This can be written explicitly with cosines as

$$a_j = \frac{1}{2N} \sum_{k=0}^{4N} A_k \cos \frac{\pi k j}{2N} \quad \text{for } j\text{=0 – N} \tag{4.4}$$

$$A'_l = a_0 + a_N(-1)^l + 2 \sum_{1}^{N-1} a_j \cos \frac{\pi j l}{N} \tag{4.5}$$

or it can be coded with FFTs.

A simple-minded FFT-based algorithm for a DCT of a $(2^N + 1)$-element, real vector, x_i, is based upon the FFT of a complex vector, X of length 2^{N+1}. The first half-plus-one of the real part of X is x. The second half-minus-one of X is all of the elements of x except the first and last, in reverse order. The imaginary part of X is zero. Each element of x appears twice in X except the first and last element, which each appear once. After performing an FFT on X, the first half-plus-one of the real part of the result is the desired DCT(x). The imaginary part of the result should be zero, to numerical precision, or you have done something wrong. This algorithm calculates many values which are thrown away, so it is not maximally efficient, but it's cost scales as $(N+1)\log(N+1)$, so it should be an improvement over the brute-force method.

We want to normalize this set of linear operations, so that if the input, R, were spectrally flat (R_{1K}) then the outputs would all be spectrally flat (T_{1K}). This means the channel normalizations can be calculated

$$B = (R_{1K} \star L)P, \tag{4.6}$$

followed by forward-transform, truncation and back-transform, as above. However, convolution with a spectrally flat R_{1K} is the same as multiplication by a delta function in the time domain, so $B = P$ and the normalization is

$$B' = \mathrm{DCT}_{129}^{-1}(\mathrm{DCT}_{513}(P))) \tag{4.7}$$

The calibrated, convolved channel radiances are

$$T_k = A'_k / B'_k \tag{4.8}$$

Coefficients l and P (both length 513) and B' (length 129) are tabulated for each of the five DACS bands. This frequency convolution requires two DCT transform pairs, the first in the convolution $R \star L$ and the second in the "sinc convolution." If the high-frequency (above lag 128) information in P is negligible, then we can make an approximation, $(R \star L)P \approx (RP) \star L$. If we make this approximation, then we do not have to come back out of the time domain to do the multiplication with P, and we can eliminate a DCT-DCT^{-1} pair. Furthermore, we are not required to make up data for the fine structure of the local oscillator shape, L, since we only need 129 lags. To get A':

- multiply R and P
- DCT_{513}(RP)
- truncate to 129 lags
- multiply by L(0:128)

- DCT_{129}^{-1}

Normalization is slightly different in this case because, in this recipe, we have multiplication by L(0:128) in the time-domain, but the difference between the two normalizations is less than one part in 10^6 for real DACS data. The differences in the radiances computed with these two methods for DACS channels of interest are on the order of 0.1 K or smaller, and the second method will generally be used in production.

The forward model for a DACS band is calculated on a "pre-frequency grid" that captures the Physics, and then is interpolated to the much larger grid of frequencies needed for filter interpolation. If these frequencies are fixed for a given tangent height, then all of the steps above, including spline or linear interpolation, are constant linear operations on the vector of "pre-frequency-grid" forward model results. For example, if we are always going to do radiative transfer on a set of 15 frequencies for a particular tangent height, we can pre-compute a 15×63 matrix that will give us the forward model channels we require. This sort of thinking might be useful in reducing the dimensionality in the retrieval problem. If we really believe that the physics of the measurement is captured in 15 numbers (or one), perhaps we should save the retrieval the trouble of sifting it out of 63 numbers.

Chapter 5

Polarized L2PC Model

The MLS level-2 retrieval software requires Jacobians of partial derivatives of the radiances with respect to state vector elements. Unfortunately, the cost of producing the polarized derivatives during routine processing is probably prohibitive. Level-2 Precomputed (L2PC) files of radiances and their derivatives for climatological conditions are used to take these calculations off-line and allow them to be calculated once, rather than for every iteration of the forward model in level 2.

Polarized L2PCs of temperature derivatives for DACS bands 22 and 26 are calculated on a grid of magnetic field strengths and orientations. In the initial versions of this code, the closest bin to the field strength and elevation angle (the angle between the field and the line-of-sight) is used. The azimuth angle can be handled analytically, since the 2x2 power spectrum coherence matrix, $\boldsymbol{I}$, or any of its derivatives, may be rotated to give values for any azimuth angle, ϕ. Since $\boldsymbol{I}$ is Hermitian,

$$\boldsymbol{I} = \begin{bmatrix} I_{\parallel} & I_{|} + \imath I_{\circ} \\ I_{|} - \imath I_{\circ} & I_{\perp} \end{bmatrix} ,$$

$\boldsymbol{I}_{\parallel}(\phi)$ can be written

$$\boldsymbol{I}_{\parallel}(\phi) = \cos^2(\phi)\boldsymbol{I}_{\parallel}(0^\circ) + \sin^2(\phi)\boldsymbol{I}_{\perp}(0^\circ) + 2\cos(\phi)\sin(\phi)\boldsymbol{I}_{|}(0^\circ) \tag{5.1}$$

With a modest bit of trigonometry, this may be recast as in terms of double-angle sines and cosines, and in terms of $\boldsymbol{I}_{\parallel}$ for three values of ϕ rather than three components of $\boldsymbol{I}$ for $\phi = 0$.

$$\boldsymbol{I}_{\parallel}(\phi) = \frac{1 + \cos(2\phi) - \sin(2\phi)}{2}\boldsymbol{I}_{\parallel}(0^\circ) + \frac{1 - \cos(2\phi) - \sin(2\phi)}{2}\boldsymbol{I}_{\parallel}(90^\circ) + \sin(2\phi)\boldsymbol{I}_{\parallel}(45^\circ) \tag{5.2}$$

This formulation is particularly useful because the forward model software is designed to select the parallel ($\parallel$) component of the radiance or radiance-derivative tensor, and to send arrays of these real, scalar values through the antenna convolution and passband convolution of the host scalar model. The polarized code can be run for $\phi = 0^\circ$, 45° and 90°, and these values may be added as in 5.2 to produce a model for any ϕ.

In its current configuration, the polarized L2PC model assumes a constant geomagnetic field magnitude and orientation along the integration path. This permits the model to be parameterized by the field value at the tangent point. However, the full forward model (and the real atmosphere) have geomagnetic-field variations along the path with resulting

radiances which cannot be modeled with a constant field. For example, changes in the field magnitude will move the $\sigma_{\pm}$ components in and out, resulting in a broadened spectral feature and weighting functions with dependence on the details of the field along the path. The degree to which this is going to cause problems in the EOS-MLS retrievals is an area for further research.

Appendix A

Matrix Exponentiation and Derivatives

By applying the Hamilton-Cayley theorem ("A matrix satisfies its characteristic polynomial") to the Taylor series for a function of a matrix, one can develop Sylvester's identity. In the case of a function of a 2×2 matrix A whose eigenvalues are z_1 and z_2 we have for any function $F()$ (in this case: exp())

$$F(\mathbf{A}) = \frac{F(z_1)}{z_1 - z_2}(\mathbf{A} - z_2\mathbf{I}) + \frac{F(z_2)}{z_2 - z_1}(\mathbf{A} - z_1\mathbf{I})$$

or

$$F(\mathbf{A}) = \frac{F(z_1)(\mathbf{A} - z_2\mathbf{I}) - F(z_2)(\mathbf{A} - z_1\mathbf{I})}{z_1 - z_2} \tag{A.1}$$

where $\mathbf{I}$ is the 2×2 identity matrix,

Now, rearrange this to get $e^{z_2}\left[\frac{e^h-1}{h}(\mathbf{A} - z_2\mathbf{I}) + \mathbf{I}\right]$. where $h = z_1 - z_2$. This is well behaved as $h \to 0$, so we don't need to futz with L'Hôpital's rule. Since $\lim_{h\to 0}\frac{\mathrm{d}}{\mathrm{d}h}\frac{e^h-1}{h} = 1$, the relative error in the first term is no greater than the relative error in h when h is small.

This could also be written as $e^s\left[\frac{\sinh d}{d}(\mathbf{A} - s\,\mathbf{I}) + \cosh d\,\mathbf{I}\right]$, where $s = \frac{1}{2}(z_1 + z_2)$ and $d = \frac{1}{2}(z_1 - z_2)$. This is useful to compute the derivative without getting into trouble as $d \to 0$, but the present form is OK here, and more efficient.

If you assume that $\mathbf{A}$ is a function of some parameter p, and work through $\frac{\mathrm{d}F(\mathbf{A})}{\mathrm{d}p}$ you will eventually find $\frac{\mathrm{d}z_1}{\mathrm{d}p}$ and $\frac{\mathrm{d}z_2}{\mathrm{d}p}$. These derivatives approach infinity as the eigenvalues approach each other. Using $s = \frac{1}{2}(z_1 + z_2) = \frac{1}{2}\mathrm{Tr}(\mathbf{A})$ and $d = \frac{1}{2}(z_1 - z_2) = \sqrt{s^2 - \det(\mathbf{A})} = \sqrt{h}$, this can be rewritten as $\exp(\mathbf{A}) = e^s\left[\frac{\sinh d}{d}(\mathbf{A} - s\,\mathbf{I}) + \cosh d\,\mathbf{I}\right]$. After much work you will find

$$\begin{aligned}\frac{\mathrm{d}\exp(\mathbf{A})}{\mathrm{d}p} = \; e^s \Bigg\{ &\frac{\sinh d}{d}\left[s'\mathbf{A} + \mathbf{A}' + (\frac{h'}{2} - s's)\mathbf{I}\right] + \\ &\frac{d\cosh d - \sinh d}{d^3}\left[\frac{h'}{2}\mathbf{A} + (hs' - \frac{h'}{2}s)\,\mathbf{I})\right]\Bigg\} \; .\end{aligned} \tag{A.2}$$

Collecting terms, we have

$$\frac{\mathrm{d}\exp(\mathbf{A})}{\mathrm{d}p} = e^s \left\{ \left[s' \frac{\sinh d}{d} + \frac{h'}{2} \frac{d\cosh d - \sinh d}{d^3} \right] \mathbf{A} + \frac{\sinh d}{d} \mathbf{A}' + \left[\frac{\sinh d}{d} \left(\frac{h'}{2} - s's \right) + \frac{d\cosh d - \sinh d}{d^3} \left(hs' - \frac{h'}{2} s \right) \right] \mathbf{I} \right\} \tag{A.3}$$

As the eigenvalues coalesce, no cancellations occur, and no infinities arise if the elements of $\mathbf{A}$ and $\mathbf{A}'$ are finite. The h' and s' terms are clearly well behaved as the eigenvalues coalesce. To see that the functions of d are well behaved, write

$\frac{\sinh\, d}{d} = \sum_{k=0}^{\infty} \frac{d^{2k}}{(2k+1)!}$ and $\frac{d\cosh d - \sinh d}{d^3} = \sum_{k=0}^{\infty} \frac{d^{2k}}{2^k k!(2k+3)!!}$, where $(2k+3)!! = 3 \cdot 5 \cdot 7 \cdots 2k+3$.

We can write $\frac{\sinh d}{d}$ as $e^{-d}\, \frac{e^{2d}-1}{2d}$ and use the same software to evaluate this expression as is used to do the matrix exponentiation. The series for $\frac{d\cosh d - \sinh d}{d^3}$ converges extremely rapidly for small d.

Appendix B

Results of Simulations

The following figures are examples of simulated radiances for MLS channels, both for canonical field orientations and for field orientations typical of an orbit.

Figure B.1: This figure shows simulated, noise-free, Band 22 radiances for $\mathcal{B} = 0.5$ Gauss in three canonical orientations (top row) and three intermediate orientations (bottom row.) Panels show pointings with tangent points from 90 km to the surface. The Doppler-broadened cores of the lines are fully saturated even in the top-most scan positions. In the top left panel, we look along $\mathcal{B}$ and the highest-altitude pointings show two fully saturated $\sigma_{\pm}$ lines. They are circularly polarized, so half of the contribution into our linearly-polarized antenna comes from the cosmic background. In the top middle panel, $\mathcal{B}$ is aligned with the antenna's $\hat{\mathcal{E}}$ direction and we see the $\sigma_{\pm}$ lines co-polarized with the antenna. In the top right panel, $\mathcal{B}$ is aligned with the antenna's $\hat{\mathcal{H}}$ direction and the π line is co-polarized with the antenna.

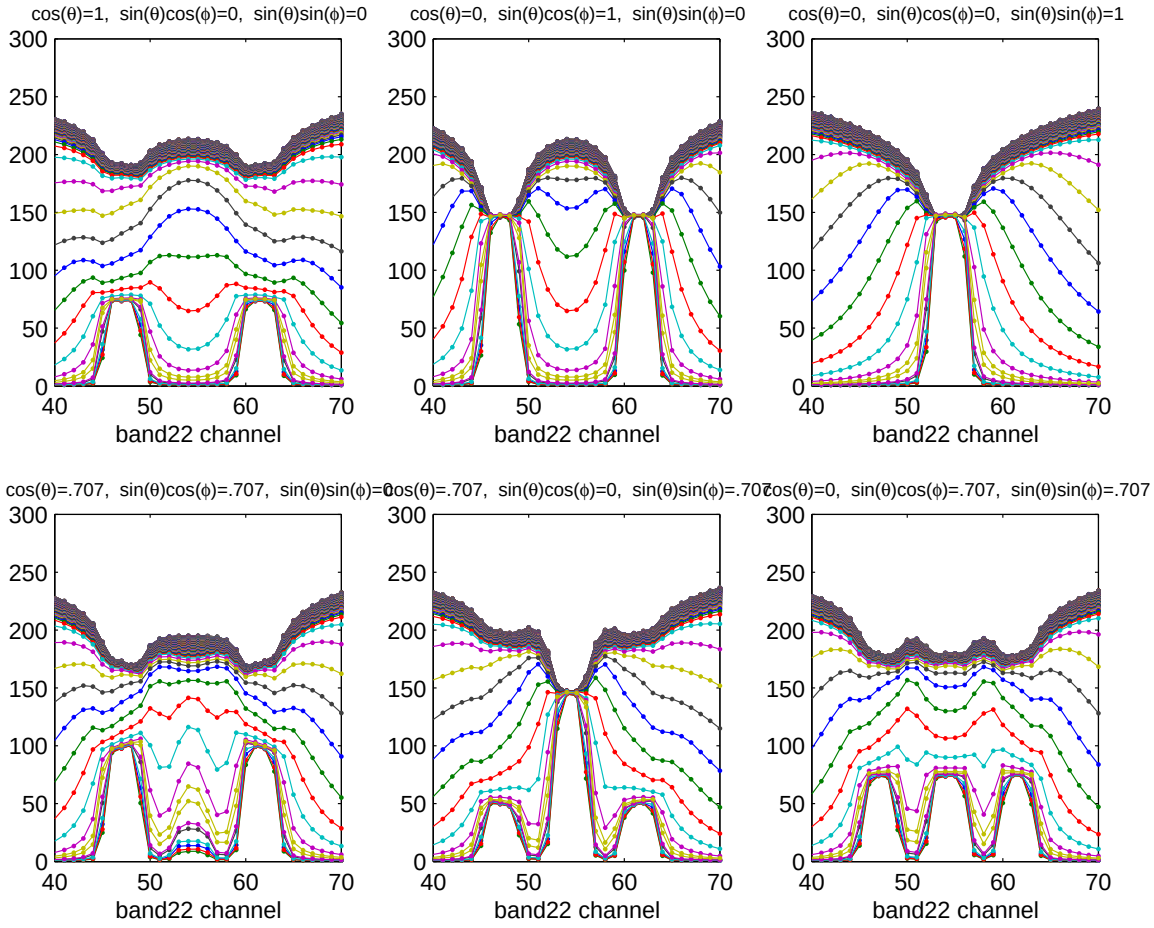

Figure B.2: This figure shows simulated, noise-free radiances for R1A and R1B for the northernmost point in the first orbit for a 1996d051 simulation (f32.) Channels listed in frequency order, with the top figure showing band 32 , band 1, and the center 6 MHz of band 22 and the bottom figure showing band 34 , band 21, and the center 6 MHz of band 26. The $\hat{H}_{\mathrm{RF}}$vector of R1B is close to the direction of the geomagnetic field, $\boldsymbol{\mathcal{H}}_{\mathrm{geo}}$, so we see the π line in R1B. We see the two σ lines, linearly polarized, in R1A.

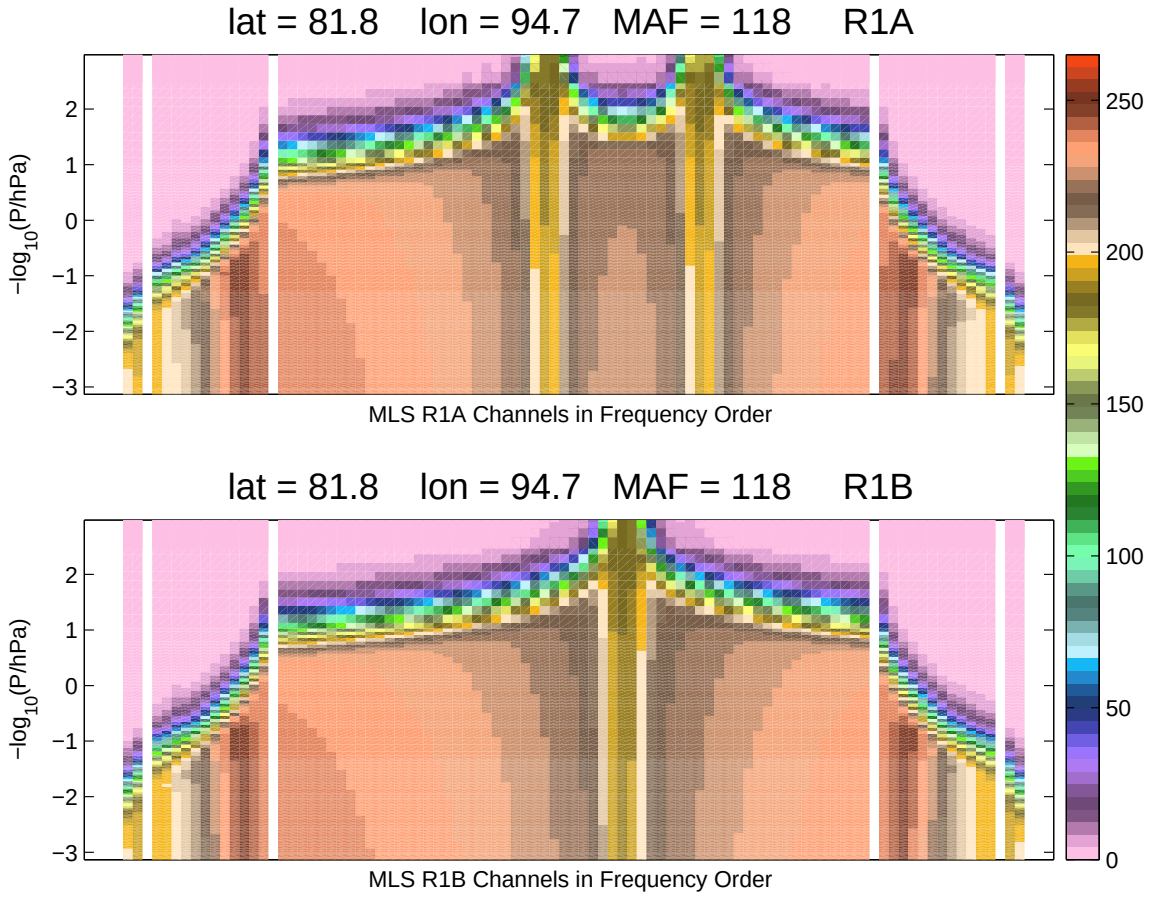

Bibliography

[1] Version 2.0 SDP toolkit users guide for the ECS project. Technical Report 333-CD-100-102, Raytheon Systems Company, Upper Marlboro, MD, January 1999. Prepared under contract NAS5-60000, CDRL item 062.

[2] C. E. Barton. International geomagnetic reference field: The seventh generation. (49):123 – 148, 1997.

[3] M. Mandea et al. International Geomagnetic Reference Field - epoch 2000 revision of the IGRF for 2000 - 2005. *http://www.ngdc.noaa.gov/IAGA/wg8/igrf.html*, 26 May 2000.

[4] John D. Jackson. *Classical Electrodynamics*. Wiley, second edition, 1975.

[5] R. F. Jarnot, R. E. Cofield, H. M. Picket, and P. C. Stek. EOS MLS instrument calibration report. Technical Report JPL D-26280, Jet Propul. Lab., Pasadena, Calif., March 30 2004.

[6] William B. Lenoir. Propagation of partially polarized waves in a slightly anisotropic medium. *Journal of Applied Physics*, 38(13), 1967.

[7] William B. Lenoir. Microwave spectrum of molecular oxygen in the mesosphere. *Journal of Geophysical Research*, 73(361), 1968.

[8] M. Mizushima. *The Theory of Rotating Diatomic Molecules*. John Wiley and Sons, 1975.

[9] R. L. Poynter and H. M. Pickett. Submillimeter, millimeter, and microwave spectral line catalog. *Applied Optics*, 24:2335–2240, 1985. http://spec.jpl.nasa.gov/.

[10] W. G. Read and Zvi Shippony. EOS MLS forward model algorithm theoretical basis document. Technical Report JPL D-18130, Jet Propul. Lab., Pasadena, Calif., March 30 2004.

[11] Philip W. Rosenkranz. Shape of the 5 mm oxygen band in the atmosphere. *IEEE Transaction on Antennas and Propagation*, AP-23(4):498–506, July 1975.

[12] Philip W. Rosenkranz and David H. Staelin. Polarized thermal microwave emission from oxygen in the mesosphere. *Radio Science*, 23(5):721–729, September–October 1988.

[13] Brad J. Sandor and R. Todd Clancy. Mesospheric observations and modeling of the Zeeman split 233.9 GHz $^{18}O^{16}O$ line. *Geophysical Research Leters*, 24(13):1631–1634, 1997.

[14] Z. Shippony and W. G. Read. A highly accurate Voigt function algorithm. 50:635–646, 1993.

[15] A. Stogryn. The magnetic field dependence of brightness temperatures at frequencies near the O_2 microwave absorption lines. *IEEE Transactions on Geoscience and Remote Sensing*, 27(3):279–289, May 1989.